



Universiteit Utrecht

Observations of the D" discontinuity, using ScS and its SdS pre cursors and interpretation in terms of the perovskite to post-perovskite phase transition.

Marialena Konstantellou

March, 2021

MSc Thesis

Supervisors:

Prof. Dr. Arwen F. Deuss

Dr. Laura J. Cobden



Abstract

One of the most controversial topics for deep earth scientists, has been the presence of the D" reflector, located a few 100km above the Core-Mantle Boundary. The main reason behind the controversy lies in the nature and the topography of this discontinuity. There are many different explanations for the existence of this discontinuity, but the dominant one is based on the phase transition from perovskite to post-perovskite occurring at similar depths. Research conducted throughout the past 40 years, have used body waves in order to investigate the presence of this discontinuity. A large number of studies is based on the SdS (or PdP) phase, which is an intermediate phase between the S and ScS phases, generated by reflection off the D" discontinuity and usually made visible by stacking all seismograms available for a specific event. The purpose of this study is to give further insight to observing the D" discontinuity with the use of shear waves and investigate if stacking is indeed required or not. A total of 16 South American earthquakes, recorded at North American stations, were used in order to cover the region of the Cocos plate. Most of these events had been studied before, but we found a new event which occurred in 2008 for which SdS was clearly visible on single seismograms. We tested the possibility to use a single seismogram method to observe the SdS reflections and measure the corresponding D" discontinuity topography, as opposed to the stacking method used in prior studies. We compared the results obtained by the two different methods and found that in some cases single seismograms can be used to determine the D" topography. We imaged the D" discontinuity and concluded to an average depth of 2690km. Furthermore, strong evidence of a varying depth from 100 to 250km above the CMB was found, along with large geographical variations in topography. Last but not least, we compared the calculated depth of the D" discontinuity with the depth in which the phase transition from perovskite to post-perovskite occurs and found a correlation, but not an absolute one since the results show a shift. Therefore, we try to also explain this shift and interpret the discontinuity's generation both as a result of the phase transition, but also as a result of slab subduction.



Contents

1	Introduction	3
2	Methodology	5
2.1	Seismic data	5
2.2	Processing	7
2.2.1	Pre-Processing	7
2.2.2	Phase Picking	7
2.2.3	Filtering	9
2.2.4	Reflection Points	11
2.2.5	Calculation of D" discontinuity depth	11
2.2.6	Stacking	13
3	Results	14
3.1	Single Event Picks	14
3.2	Stacking	17
3.2.1	2000 event	18
3.2.2	2008 event	18
3.2.3	Amplitude Ratios	24
3.3	Comparison with tomography	24
3.3.1	S20RTS	25
3.3.2	S40RTS	27
4	Discussion	29
5	Conclusions	31
6	Acknowledgments	32
7	References	33
8	Appendix	36



1 Introduction

One of the most revolutionary observations concerning the deep Earth, has been the discovery of the D" discontinuity. The first introduction to the D" layer was done by [Dahm, 1934] and was later given its name by [Bullen, 1949]. After this discovery, numerous studies have been conducted in order to locate and image the D" discontinuity. For, at least, 40 years now many studies have observed a sudden change in seismic wave velocity right above the Core-Mantle Boundary (CMB). The existence of the discontinuity is based on the sharp increase in the shear wave velocity (δV_S), which can even reach the value of 4%, as well as a smaller increase in the P-wave velocity (δV_P) [Wookey et al., 2005], [Wentzcovitch et al., 2006], [Hirose et al., 2007], [Stackhouse and Brodholt, 2007]. Moreover, a shear wave triplication in the lowermost hundred kilometers of the mantle, was another evidence for the existence of the D" discontinuity [Lay and Helmberger, 1983]. Until this day, several studies have successfully imaged the D" discontinuity using different seismic waves and methods of processing [Lay and Garnero, 2011]. In some studies, P-waves are used, whereas in some others shear waves are used instead. Shear waves tend to be a better candidate for studies involving the deep mantle, due to the fact that discrete phases are more easily detected because they are longer period waves compared to the P-waves.

The geographical distribution, the depth and thickness of the D" discontinuity which are widely varying, are some

of the main reasons why the D" discontinuity is so intriguing. More precisely, the depth of the D" discontinuity appears to vary from 100km up until 450km above the CMB, even though the average depth of the discontinuity is calculated to be approximately 260km above the CMB [Cobden and Thomas, 2013]. Estimates of the thickness range from 8km and up until 100km [Weber, 1993, Wyssession et al., 1998, Lay, 2008]. Apart from the variations in the depth and the thickness of the discontinuity, the non-uniform presence of the discontinuity leads to an additional difficulty in its research.

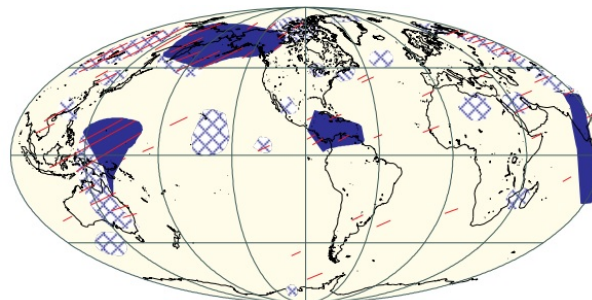


Figure 1: Locations where shear-wave discontinuity near the top of the D" layer was observed. The blue areas represent regions with large-scale coherence, red lines represent regions where we lack extra reflections and cross-hatched areas represent areas where the D" does not appear continuous. Image by *Lay et al., 1998*.

This means, that the discontinuity does not appear everywhere in the world [Weber, 1993], [Kendall and Nangini, 1996], [Chambers and Woodhouse, 2006]. This can be also seen on **Figure 1**, as reviewed by [Lay et al., 1998], regions with large-scale coherence are plotted as blue, the areas



where there is a lack of extra reflections are plotted as red lines, while the regions where the D" is not continuous and varies are plotted as cross-hatched.

Additionally, an explanation for the generation of the D" reflector still remains unanswered. There are some explanations which could possibly explain under what circumstances and why the D" layer was created. The discontinuity could be a product of subducted slabs, which cause a decrease in the temperature and an increase in the velocity. Chemical heterogeneity seems to be another plausible answer for the origin of the discontinuity. Lastly, the most dominant scenario suggests that the discontinuity is caused by the phase transition from perovskite ($(Mg, Fe)SiO_3$) to post-perovskite [Hirose et al., 2007]. This phase transition occurs at pressures of approximately 120 GPa and 2500K, which corresponds to a depth of 2600km, coinciding with the depth where the discontinuity is observed. This phase transition was discovered because of a robust change in the X-ray diffraction (XRD) pattern at those temperatures and pressures.

In this study, we will use the SdS arrival in order to detect the reflection off the D" discontinuity. SdS is an intermediate phase between the direct S wave (which turns in the mantle) and the ScS wave (which reflects off the CMB). Therefore, this phase is also expected to have an intermediate traveltime and slowness. A schematic representation of the ray paths of these three phases, can be seen in **Figure 2**.

In order to actually observe this secondary phase, the epicentral dis-

tance must be in the range between 70 to 83 degrees so that the discontinuity produces strong enough secondary arrivals between the major S and ScS phases [Lay and Garnero, 2011, Wyssession et al., 1998]. Since we want to reduce the effect of attenuation as much as possible and therefore obtain more clear peaks, intermediate and deep focus events were chosen, with a depth which is larger than 200km.

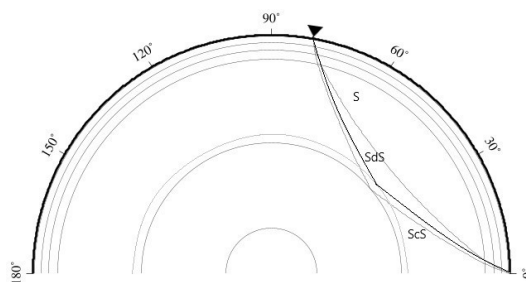


Figure 2: Ray paths of the seismic phases S, SdS and ScS which were used in this project. S turns in the mantle, ScS reflects off the CMB, while SdS reflects off the D" discontinuity.

The main difference between this project and the previous studies (for example [Lay et al., 2004], [Thomas et al., 2004], [Cobden and Thomas, 2013], [Lay and Garnero, 2011] etc.) is the fact that we wanted to observe the SdS phase only with the use of single seismograms. It is quite challenging to use only single seismograms for the observation of secondary phases, that is why the past studies used extra processing steps which can complement and enhance the information, by stacking, resulting in vespagrams and even fourth root vespagrams. Considering all those facts, it is understandable that we will show that some



events which showed clear SdS peaks in stacks in previous studies, did not always show SdS in single seismograms. However, we were lucky to find a new event which showed very clear SdS arrivals in single seismograms and we study it in detail. Despite those challenges, we successfully observed the ScS precursor and imaged the D" discontinuity using the new event and also in some of the events from the previous studies. The vespa process, was used as an extra step, in order to compare and discuss the different results obtained from the two methods. Finally, based on our results we made a correlation with the phase transition from perovskite to post-perovskite which occurs similar depths.

2 Methodology

2.1 Seismic data

Firstly, we downloaded the data from the IRIS website, using the Wilber 3 data request. For this project, 16 events were used in total (see **Table 1**), 12 of which have already been studied in the research conducted by [Lay et al., 2004], as well as, [Thomas et al., 2004]. Those 12 events are from the time period of 1991 up until 2001. All of the events are located in the subduction zone of South America and recorded at stations in North America (see **Figure 3**). The ScS reflection points appear to be localized in the region of the Cocos plate. This localization occurs at latitudes from -3 to 20 degrees and longitudes from -90 to -80 degrees, therefore this will be the area of focus.

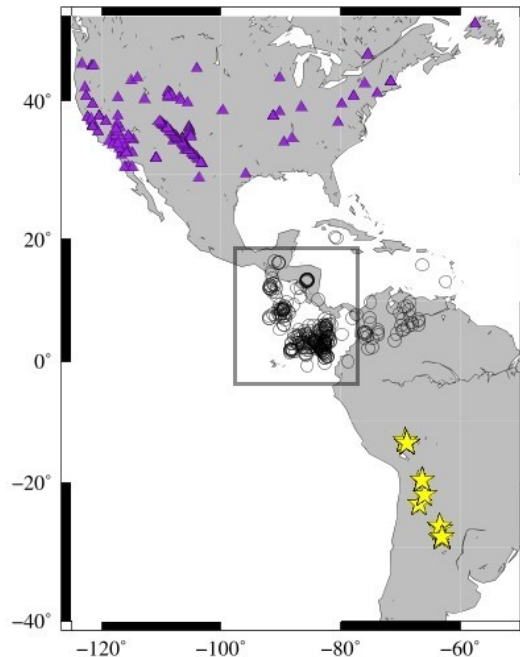


Figure 3: Map projection of the 13 events (stars), the stations (triangles) and reflection points (circles), for all of the 13 events used in this study. The region which will be the focus of this study is included in the grey square.

The earthquakes are of intermediate and deep depth, therefore they have their epicenter at a depth greater than 200km. The epicentral distance range (distance between the event and each station), has to fall within the range of 65 to 83 degrees. Even though the ideal epicentral distance to observe the SdS arrival, is from approximately 75 to 83 degrees, we also included some smaller distances. This was a good choice, because we also observed the SdS phase at smaller distances, but this is a rare occasion and it is an exception to the rule. Moreover, all of the events must have moment magnitudes greater than 5, otherwise there is not enough energy to produce a clear enough SdS phase. Lastly, we downloaded data from only the BHN and BHE channels, because the horizontal



component seismograms best record the S and ScS phases. The data for each event is collected from 0 seconds before event time up until 30 minutes after event time.

Apart from those 12 events, which had been studied before [Lay et al., 1998], we tried to find new events to complement our study. In order to find new events, we first had to choose the specific area of interest, by choosing the desired latitude and longitude. The previously studied earthquakes are located in South America and were recorded by North American stations, therefore we based our selection to this information. We continued by choosing the event depth to be larger than 200km and an epicentral distance range from 65-83 degrees. After finding a good

event, we proceeded to download half an hour of data, as mentioned above. It was quite hard to find an event good enough to include in this study, because not all of them showed an SdS arrival between the S and ScS phases. We searched for events which took place after 2001, which was the last year included in prior studies. We found events from the time period of 2002, up until 2018. Additional events from 2002, 2007 and 2018, were studied and rejected because no SdS was visible on single seismograms. Due to the limited time, we did not study the rest of the events which we have downloaded. After some research, we were able to find a new event that was used in order to enrich this study.

Event	Date	Latitude	Longitude	Depth	SdS observations
1	June 23rd, 1991	-26.82	-63.40	570.3	1
2	May 24th, 1993	-23.45	-66.88	231.9	1
3	October 19th, 1993	-22.12	-65.69	278.9	1
4	January 10th, 1994	-13.28	-69.27	603.6	4
5	April 29th, 1994	-28.51	-63.22	565.9	5
6	May 10th, 1994	-28.62	-63.02	603	4
7	July 20th, 1997	-22.82	-66.12	271.3	0
8	August 19th, 1994	-26.72	-63.42	562.6	2
9	January 23rd, 1997	-22.04	-65.92	281.6	3
10	November 28th, 1997	-13.70	-68.90	600.5	18
11	April 23rd, 2000	-28.41	-63.04	607.9	37
12	June 19th, 2001	-19.68	-66.39	287.2	9
13	March 28th, 2002	-21.69	-68.57	137.8	0
14	July 21st, 2007	-22.31	-66	280.2	0
15	September 3rd, 2008	-26.85	-63.3	571.3	60
16	August 24th, 2018	-11.18	-70.82	627.7	0

Table 1: Events used in this study.



2.2 Processing

2.2.1 Pre-Processing

The first step of the processing procedure involved the validation of the event information, which we downloaded. First, we needed to make sure that the origin time of the event, the latitude, the longitude and the depth are correct. This was done by checking the information in the Global Centroid Moment Tensor Catalog (<https://www.globalcmt.org/>) [Dziewonski et al., 1981], [Ekström et al., 2012]. We continued by removing the instrument response and converting the velocity to ground displacement, by deconvolution. For this procedure, as well as the rest of the processing steps, we used the Seismic Analysis Code (SAC) [Helffrich et al., 2013]. The next step involved the rotation of each pair of BHN and BHE components to the radial (BHR) and transverse components (BHT), respectively, for each station. The transverse component is the one that was used for the project, due to the fact that it is predominantly SH energy, while the radial component also contains P and SV energy.

2.2.2 Phase Picking

Following the rotation to the great circle path, we calculated and plot the predicted S and ScS arrival times in our seismograms, based on the AK135 Earth model [Kennett et al., 1995]. Having those arrival times as a reference, we proceeded to manually perform our own phase picking, for S, ScS and also SdS, on the transverse component seismograms. Before starting the phase picking, it is

very important to remove the mean and the trend from all seismograms. As an additional step, we multiplied all of the seismograms for which ScS had a negative amplitude with -1, because we wanted positive polarities for all the data. For the manual phase picking, we picked the maximum of each peak and not the beginning or onset of the arrivals. We continued by aligning all the seismograms on our picked ScS arrival time. In other words, this means that the ScS peak will be at $t = 0$ seconds and it will be easier to observe the SdS phase. Since there is an alignment on ScS, the time window of interest is between approximately -50 to 30 seconds. An example seismogram which is already aligned on ScS, with all the phases included, can be seen in **Figure 4**.

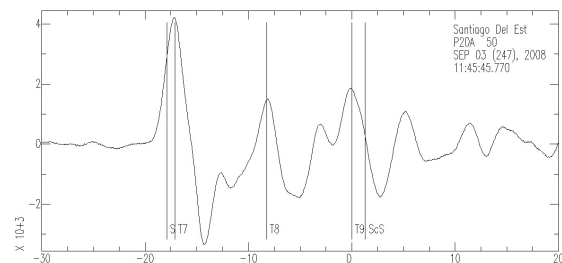


Figure 4: An example seismogram depicting the predicted and the observed arrivals of the S, SdS and ScS phases. The seismogram is from the P20A station, which recorded the 2008 event. The predicted (labeled as S, ScS) arrival times based on the AK135 Earth model are shown, as well as, the observed phases (labeled T7, T8 and T9) corresponding to the manually picked S, SdS and ScS phases, respectively.

Note that in this seismogram the SdS phase is clearly visible in a single seismogram, without the need for stacking. In the case depicted in **Figure 4**, the dif-



ferences between the predicted and the picked phases are not that great, but there are other cases where the time difference is larger. Those time differences between the predicted and the observed phases, will later be used for interpretation. As a next step, we plotted all the seismograms corresponding to an event, as a function

of epicentral distance. By doing that, it becomes quite easy to observe the additional phase between the S and ScS, since it is dependent on the epicentral distance. Data profiles in the transverse component for four different events, which have been processed are shown on **Figure 5**.

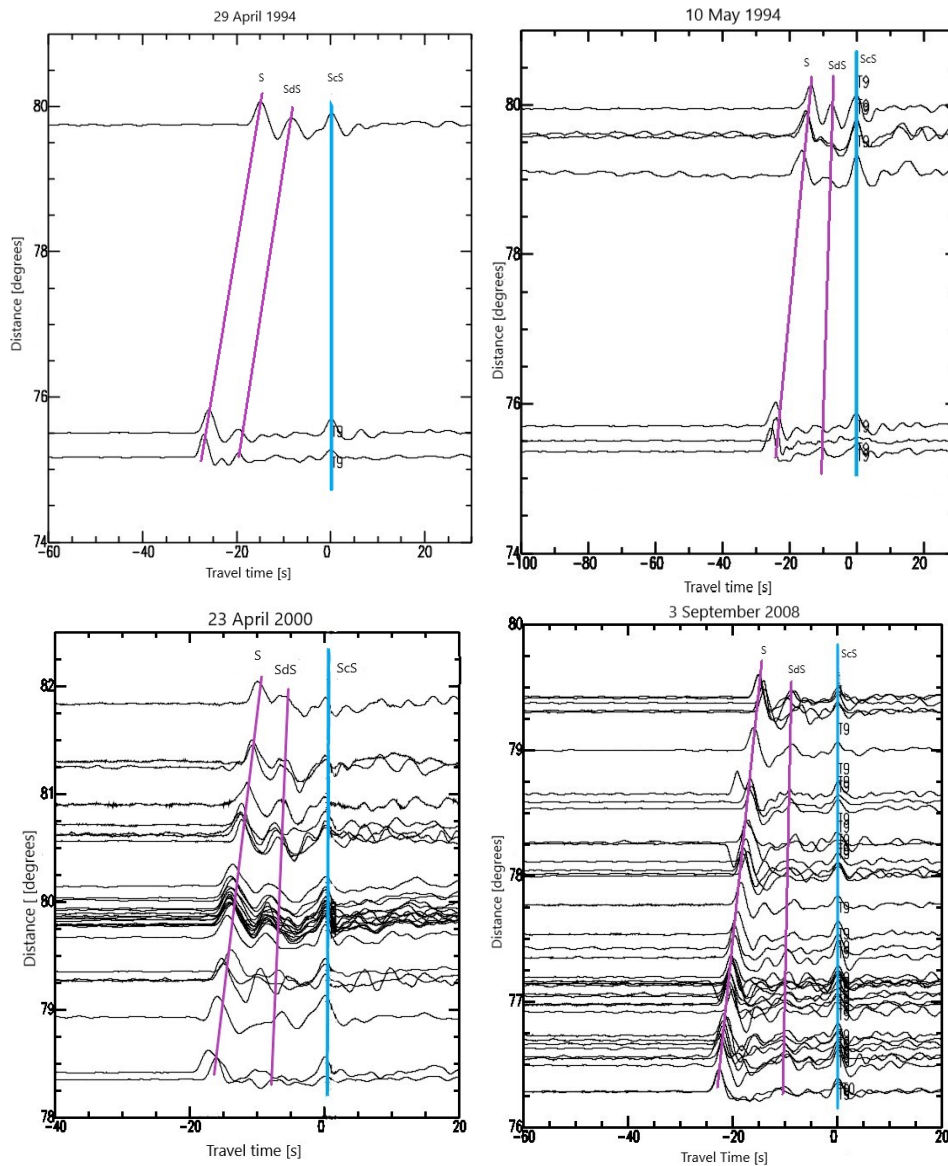


Figure 5: Data profiles of the transverse component, for four different events, which have been processed and aligned on ScS. With the blue line the ScS arrival is marked, while the S and SdS arrivals are marked with purple.



The two earlier events that took place on 29 April 1994 and 10 May 1994, only have a limited number of seismograms. The two more recent events on 23 April 2000 and 3 September 2008, show a much larger number of stations due to the more recently installed US array stations. Between the main S and ScS phases, a clear intermediate additional phase can be often observed, though definitely not for all seismograms. This additional arrival, at teleseismic distances (i.e. 75 to 83 degrees), can only be generated by the presence of the D" discontinuity, right above the CMB, resulting in the reflection phase SdS.

2.2.3 Filtering

After the removal of the trend and the mean and before picking and aligning the seismograms on ScS, the next step has been the application of filtering. In the paper by [Cobden and Thomas, 2013], a Butterworth bandpass filter between 3 and 25 seconds was applied, while in the paper by [Whittaker et al., 2015], the period of the Butterworth filter is between 1 and 20 seconds. On the contrary, in the paper by [Lay et al., 2004] and [Thomas et al., 2004], a lowpass filter with a corner at 0.3Hz was used, instead. There is no "right" filtering and one should choose depending on the needs of the study and the data. After trying all the different types used in other studies and even trying filtering with different corner frequencies, we decided that it is better if there was no additional filtering applied to the data. Important information seems to get lost when a filter is applied and this can also be seen in **Figure**

6, where the data profile of the event that took place in 2008 is plotted. The first figure is the unfiltered data, whereas on the rest of the figures, we have applied different filters to show the differences.

On the top right figure, a Butterworth bandpass filter between 0.01Hz and 0.1Hz, with 2 poles and 2 passes has been applied. It is clear, that this filter smears the data and we lose important information if not all, and therefore we can not even observe the two main phases. On the bottom left figure, we applied a Butterworth bandpass filter again, but this time between 0.04Hz and 0.33Hz and with 4 poles. We can see that this filter is better than the previous, but it still seems to cause a smoothing to the data and the phase peaks. Last but not least, we applied a lowpass filter with a corner at 0.3Hz and the result appears to be similar like the one applied before. Both the lowpass filter and the bandpass between 0.04Hz and 0.33Hz, showed good results, but we believed that the unfiltered data is more clear.

If we observe the figures more closely, we see that the peaks on the unfiltered data are more spiked compared to the differently filtered data. We should also consider the difference in the methods used. This means that for the stacking, the data should be filtered and smoothed in order to give good and clear results. On the other hand, since this study involves the observations of the SdS phase on single seismograms, if we applied filtering and made the data smoother, then we would end up with actual loss of information. The difference in the methods should always be taken into consideration when deciding the processing steps.

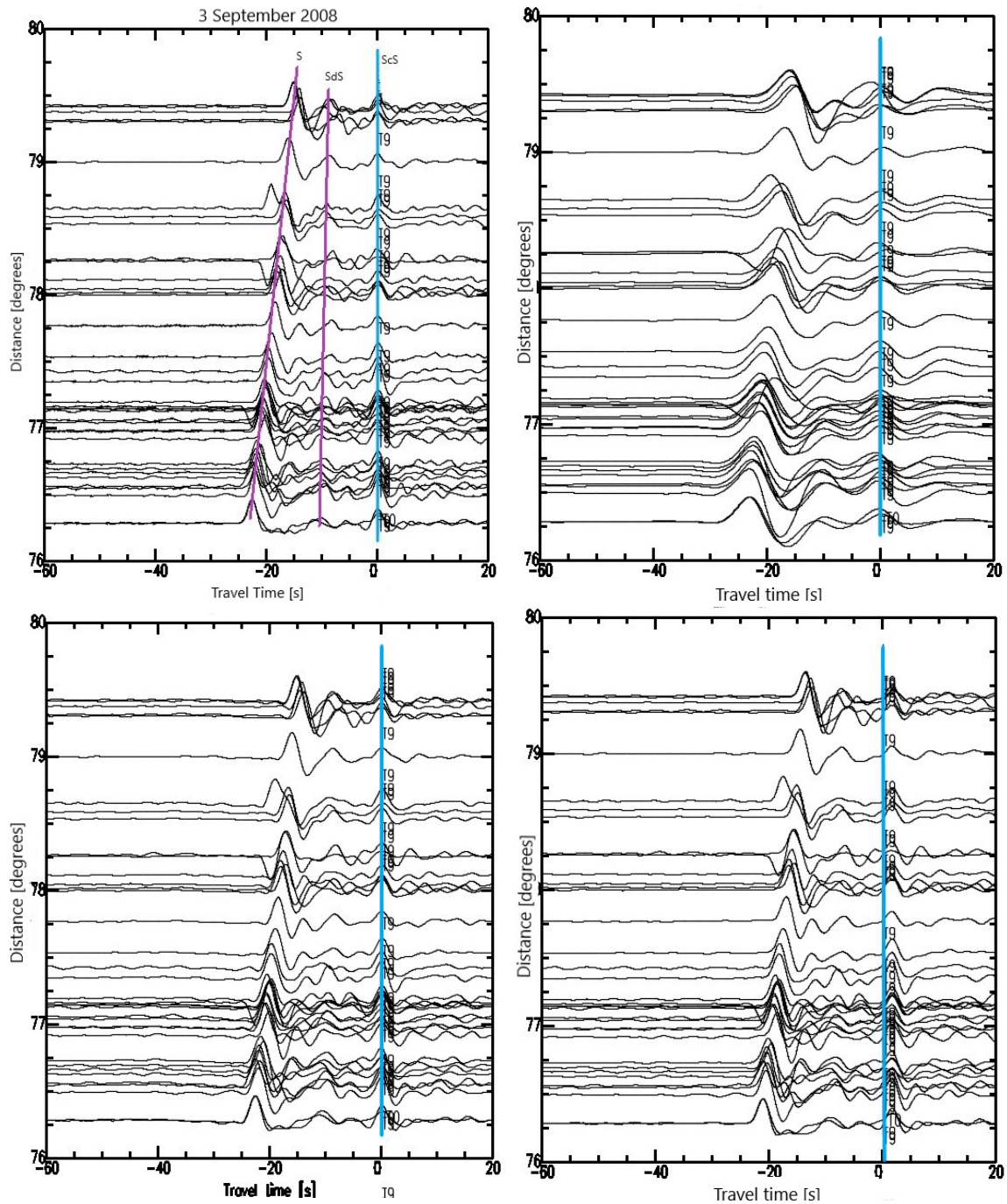


Figure 6: Four profiles of the 2008 event showing the different filters applied. The top left figure represents the unfiltered data, the top right has been filtered with a Butterworth bandpass filter between 0.01 Hz and 0.1 Hz. The bottom left figure has been filtered with a Butterworth bandpass filter between 0.04 Hz and 0.33 Hz and the bottom right with a lowpass filter with a corner at 0.3 Hz.



2.2.4 Reflection Points

Plotting the reflection points on a map in order to observe the coverage of the study area, is an important step to make interpretations. We started by creating a file which contains the following information, for each station:

1. Epicentral Distance
2. Station longitude
3. Station latitude
4. Event longitude
5. Event latitude
6. Time difference between the predicted ScS and S
7. Time difference between the observed ScS and S
8. Time difference between the observed ScS and SdS.

In order to locate the reflection points of each station, we used the TauP Toolkit [Crotwell et al., 1999]. More specifically, we used the *taup pierce* tool, which calculates pierce points at model discontinuities, but also at depths specified by the user. We chose a pierce depth of 2890km, which corresponds to the depth of the Core-Mantle Boundary. Since we are interested in the location of the D" reflector, the reflection off the CMB is expected to be right below the reflection off the discontinuity.

2.2.5 Calculation of D" discontinuity depth

As a final step, we calculated the differential times of ScS-SdS for the pre-

dicted Earth model. Since no Earth model can predict the SdS arrival time, we once again used TauP Toolkit to achieve this. We used the station's coordinates and its ScS reflection point coordinates. Those reflection point coordinates, were assumed to be the event's coordinates and its depth was assumed to be the CMB depth (2890km). From this calculation we get the ScS travel time from the CMB to the receiver, but only for one leg. We repeated the same procedure with a step of 50km, up until 2500km depth, for the same station coordinates. We do not know the specific depth of the discontinuity and that is why we repeated the procedure and considered a different D" depth, each time. This calculation gave us the SdS travel time from the D" to the receiver, for one leg.

It was also necessary to find stations which covered a wide range of epicentral distances, starting from 73.5 to 80 degrees, with a step of approximately 0.5 degrees. Example tables of various epicentral distances which were used, can be found in the Appendix section. We calculated the time difference between the ScS arrival time (which is the same for every station) and the SdS arrival time, for each step of depth (**Figure 7**). In this figure, the grey lines represent the legs that do not get calculated, whereas the black lines represent the calculated travel times for ScS and SdS. Since we need to calculate both legs, we multiply the time difference with 2 and this gives the final time difference.

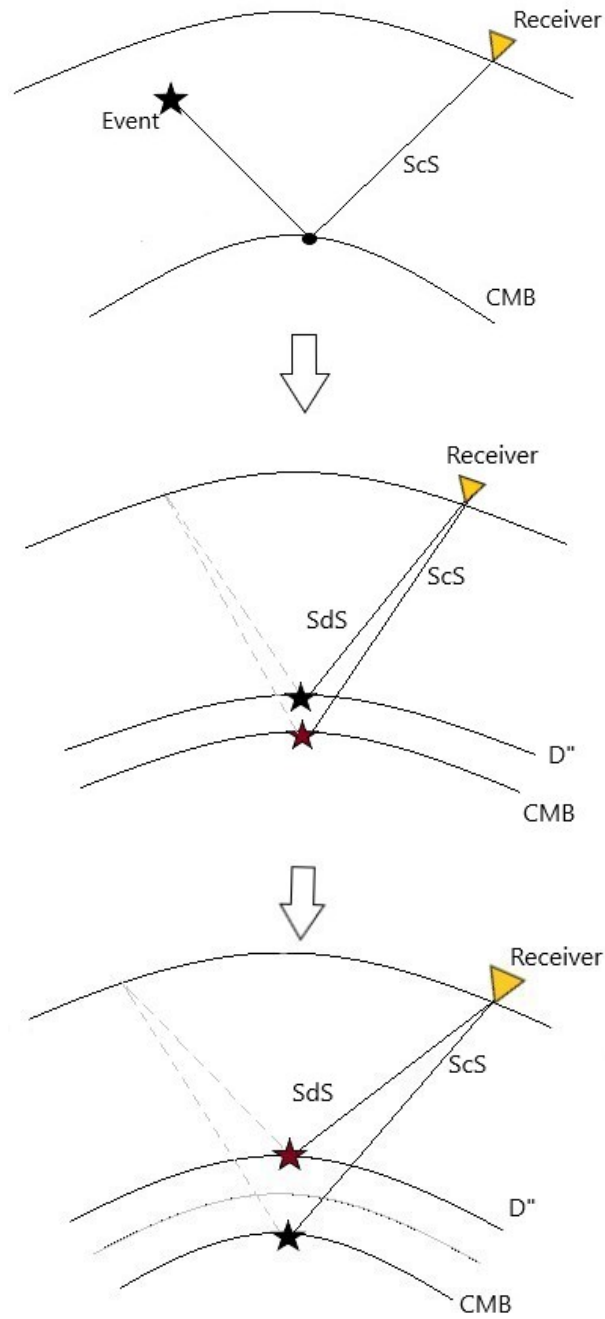


Figure 7: Schematic representation of the method used in order to make the time to depth conversion. The grey lines represent the other "leg" of the travel time, which need to be calculated.



A xy plot in order to show the time difference that corresponds to each depth, for three different epicentral distances is depicted in **Figure 8**. The green color corresponds to an epicentral distance of 73.5 degrees, the blue to 76 degrees, while the pink to 80 degrees.

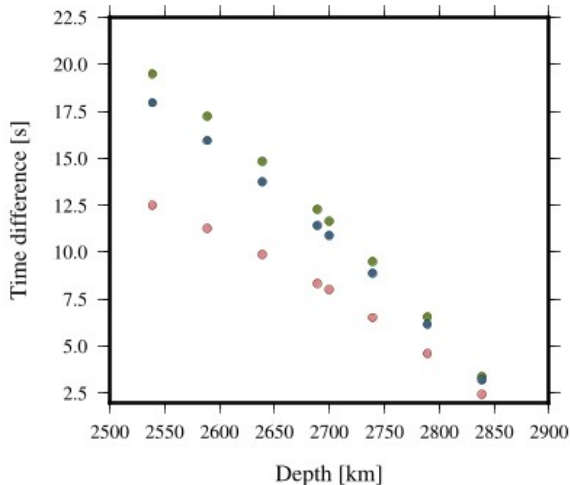


Figure 8: xy plot of the ScS-SdS time difference as a function of depth. The green color corresponds to an epicentral distance of 73.5 degrees, the blue color corresponds to 76 degrees, while the pink color to 80 degrees.

As it is expected, for smaller epicentral distances we have larger time differences between ScS and SdS. For an increasing epicentral distance, the SdS and ScS arrival times are closer and therefore their time difference is smaller. Moreover, the time difference is smaller in deeper depths, while for shallower the time differences are strongly larger. Another observation, is that for shallower depths, the time difference is strongly dependent on the epicentral distance, because in the plot we see a sudden divergence between 73.5 and 80 degrees.

With the process described above, we

calculated the ScS-SdS differential times for the predicted Earth model. For each station, we first looked at its epicentral distance and correlate it with the epicentral distances which were calculated before. Then, we could compare the ScS-SdS differential times from our picks to the ones from the predicted Earth model and conclude to the corresponding depth of the D" reflector.

2.2.6 Stacking

Since we wanted to compare the results between the single seismogram and the stacking methods, we stacked two events and produced vespagrams. A vespagram is basically a slowness stack as a function of travel time and was first introduced by [Davies et al., 1971]. The stacking process involves the time shift of the seismograms, according to their epicentral distance Δ and their slowness p . The horizontal slowness (or ray parameter) is the reciprocal of the apparent velocity [Akii and Richards, 2009]. In order to proceed with the stacking process, we needed to pick a seismogram which would be first on the list and would give the reference epicentral distance Δ_{ref} . This seismogram had to have an intermediate epicentral distance, which means that it had to be in the middle of the range of all the epicentral distances of all the stations. The time shift is given by the equation $t_{shift} = p \times (\Delta - \Delta_{ref})$.

Based on the vespagrams that we have produced, we can calculate the depth of the D" discontinuity. As explained above, in order to do the stacking we needed to select a seismogram that falls within the



middle of the epicentral distance range. From this seismogram, we got the reference epicentral distance which will be used in order to correlate it with the calculated ScS-SdS difference. For each vespagram, we needed to plot the stack which corresponds to the maximum slowness of the SdS phase. From this stack, we wanted the time at the peak of the SdS amplitude. Since the ScS phase is at $t = 0$ sec, the time of the SdS will be equivalent to the ScS-SdS time difference. With this time difference and the epicentral distance, we made the correlation to the D" discontinuity depth, the exact same way like we did in the single seismograms processing (see Appendix for reference tables).

3 Results

3.1 Single Event Picks

As expected, the single seismogram method was not always successful in the observation of the SdS phase. Even though some stations were within the epicentral distance in which we would expect to observe the additional intermediate arrival, that was not always the case. Two example seismograms are depicted in **Figure 9**. The top seismogram is from the event in June 23rd 1997, where the data was limited. We can see the main S and ScS phases but no clear intermediate phase can be observed between them. We can see a small upward trend, but it is not strong enough in order to consider it an additional phase. Furthermore, the bottom seismogram is from the event which

took place in November 28th, 1997. This is a case where not only there is no SdS phase, but the ScS phase is not strong enough. This is an example of bad data in general, which should not be taken into consideration.

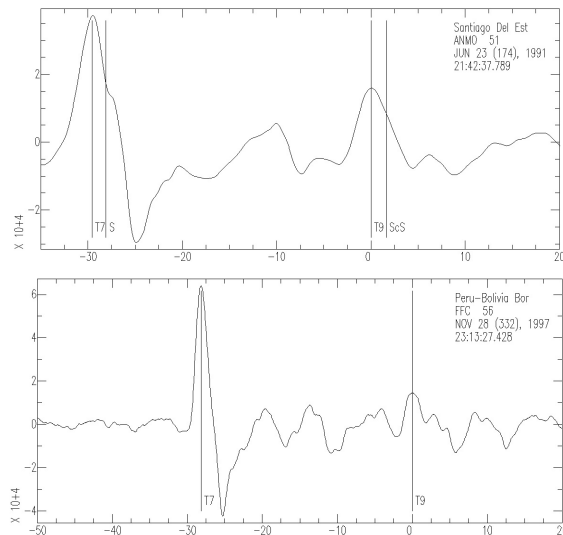


Figure 9: Example seismograms from two events that took place in 1994 and 1997, respectively.

Out of the 16 events which were processed, only 12 showed clear SdS arrival on single seismograms. On **Table 1**, the single seismogram SdS observations are listed per event. Even in this case, there were events, mostly before 1997, in which only in one seismogram the SdS arrival was observed. The profiles of all events which showed an SdS arrival, can be found in the Appendix section. For comparison, the profiles from the events that took place in July 1997 and March 2002 are also plotted in the Appendix. Those are two examples of events which show no clear SdS arrival on single seismogram.

With the use of the predicted travel times, it was quite easy to manually pick



and observe the different phases. After the phase picking and calculation of the ScS-SdS differential time, we were able to calculate the D" discontinuity depth for each reflection point. A map projection of the color coded SdS reflection points is plotted on **Figure 10**.

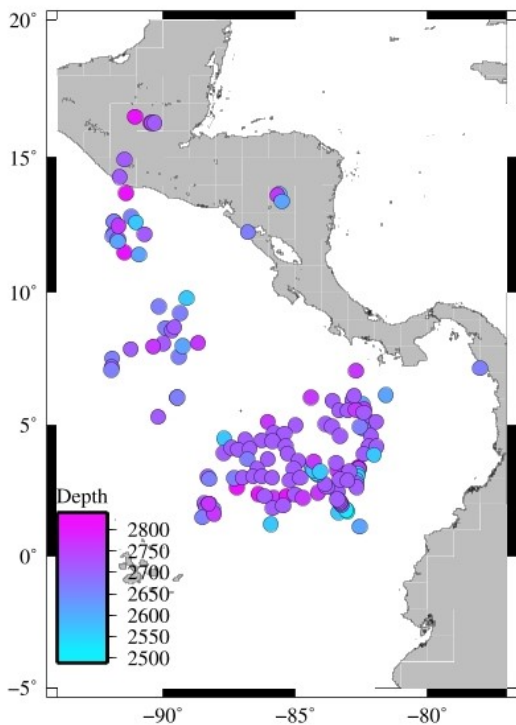


Figure 10: Map projection of the color coded reflection points for all of the events used in this study.

From the map we can see that the dominant depth of the discontinuity is between 2960-2700km. Despite this, some shallower and deeper depths are observed scattered in the region. The north part of the study area seems to have shallower depth reflectors, whereas the south part has both shallower, but also deeper reflectors.

Previous studies [Thomas et al., 2004] have showed that there is a variation

of the depth between the northern and the southern part of the region. More specifically, there is evidence that in the southern part the D" discontinuity showed greater depths compared to the northern part. In order to better see the depth variation as a function of latitude and longitude, we created two simple plots showing D" discontinuity depth as a function of latitude and longitude, starting with the latitude plot in (**Figure 11**, top). Once again we observe that the dominant depth is approximately 2690-2700km, with most of the reflection points concentrated between 0 and 10 degrees.

Based on the top plot on **Figure 11**, we subdivided the area in latitudinal bins with a step of 5 degrees and got an average depth per bin, in order to get a better image of the topography. In lower latitudes we have an average depth of 2690km, the depth increases higher latitudes, between 5 and 10 degrees, then it reduces again between 10 and 15 degrees and finally towards the north we observe the largest depth of 2790km. To get an even more detailed picture of the topography of the discontinuity, we subdivided the area in even smaller latitudinal bins with a step of 2.5 degrees, leading to 7 bins. On lower latitudes there seems to be a constant depth between 2690-2700km, while as we move towards the north the depths suddenly decrease to 2640km and then increase and reach 2790km.

If we compare our results with other studies, there seems to be a correlation, up until 15 degrees. More precisely, we observe shallower depths towards the north and deeper towards the south, agreeing with [Thomas et al., 2004]. From 15 to



17.5 degrees we can observe a deeper reflector, but if we compare with the top figure, we see that we only have 4 points located there. It is important to note, there-

fore, that both in our study and the previous study, there are only a small number of data points in the north, so a perfect comparison cannot be expected.

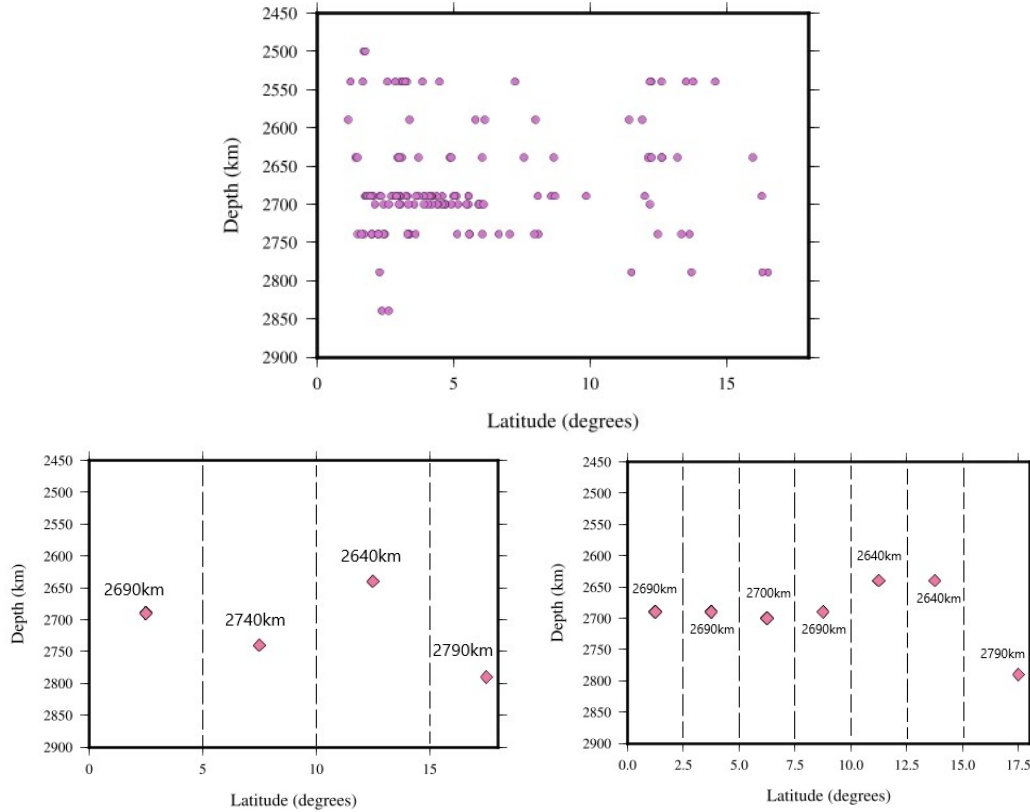


Figure 11: Top: A simple xy plot of depth versus latitude. We can see that most of the reflection points give a D" layer depth of 2690-2700km. Middle: The same xy plot, but now the area is subdivided in 4 latitudinal bins with a step of 5 degrees and get an average depth for each bin. Bottom: In order to look for more details, the area was subdivided in 7 latitudinal bins with a step of 2.5 degrees.

Similar to **Figure 11**, we followed the same procedure and therefore plotted the depth as a function of longitude. It is clear that most of the reflection points are concentrated between -93 to -81 degrees in longitude, as mentioned before. From **Figure 12, top**, it is clear that, in this case as well, the dominant depth is 2690-2700km. We subdivided the area

in longitudinal bins with a step of 5 and 2.5 degrees, in order to get a topography of the discontinuity. From the 5 degrees bin, we observe that the D" discontinuity depth is almost constant at 2690km and the only outlier is between -92.5 and -90 degrees, but the data is limited and therefore it should not be taken into consideration. The same behavior is observed in the



2.5 bins figures, where between -90 and -72.5 degrees, the depth is almost constant, while we still have the outlier before -90 degrees. Moreover, there are some gaps at the bins since there were no reflections located there.

In general, the single seismogram method seems to give good results. More specifically, we were able to locate the D" discontinuity, without the use of stacking

and in more detail since we get an individual depth per point and there is no averaging present. It was more difficult when older events were concerned, due to the limited data which reduced the probability of observing the secondary SdS phase. On the other hand, in more recent events, where the US array was installed, we had data from more stations which increased the chances of observing SdS.

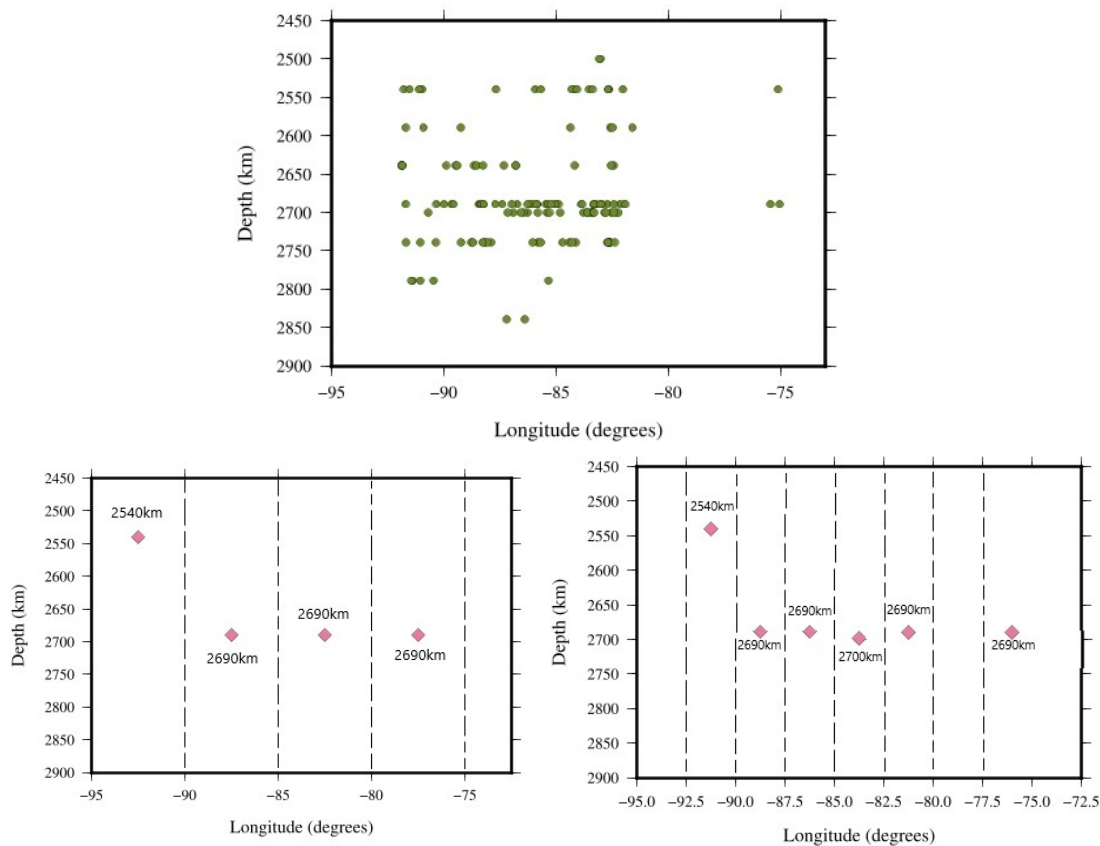


Figure 12: Top: A simple xy plot of depth as a function of longitude. Bottom: The same xy plot, but now the region is subdivided in longitudinal bins with a step of 2.5 degrees.

3.2 *Stacking*

As an additional step we decided to stack the seismograms and produce vespagrams for the 2000 and 2008 events, which were two of the events that gave good re-

sults in the single seismogram method.

In most cases the weak SdS arrivals cannot be detected on single seismograms, therefore the vespagram process is required. In all the previous studies



[Lay and Garnero, 2011], the vespagram process is used in order to make interpretations and locate the depth of the D" discontinuity. Vespagrams provide slowness information which gives further confidence that the SdS phase, which was observed on single seismograms, is indeed from the lowermost mantle. Furthermore, there are cases where the secondary SdS phase cannot even be detected on linear vespagrams and therefore fourth root vespagrams have been used, instead [Muirhead and Datt, 1976].

3.2.1 2000 event

We started by stacking the 2000 event, which has been studied before [Lay et al., 2004], [Thomas et al., 2004]. The result of the Velocity Spectrum Analysis (Vespa) is depicted on **Figure 13**.

Their maximum slownesses are marked with stars for convenience. We can see a really strong S phase arriving with a slowness of approximately 3.3 s/deg compared to ScS. We observe extremely high values of amplitudes, which could be due to the fact that the seismograms that were stacked have similar epicentral distances. If the range was wider, then the amplitudes would not be that amplified as a result of the stacking.

The ScS phase is visible and also quite strong with a slowness of 0 s/deg, since the seismograms are aligned on ScS. This means that for slowness $p = 0$, no time shift will take place, therefore leading to a maximum slowness for the ScS phase. The SdS phase, on the other hand, appears to be quite weak. The slowness of the SdS phase is equal to approximately

0.5 s/deg. This observation was also made by [Thomas et al., 2004], where they noticed that the SdS phase is really weak and even hardly visible in the 2000 event. For the 2000 event the reference epicentral distance is equal to 77.01375 degrees and therefore, the corresponding depth of the D" discontinuity is 2690km.

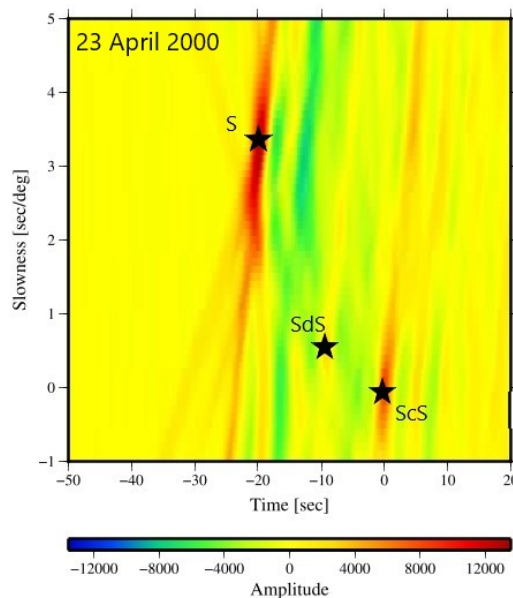


Figure 13: Vespagram of the 2000 event. The S and ScS phases appear to be quite strong, while the SdS phase seems weak. S arrives with a slowness of 3.3 s/deg and SdS arrives with a slowness of 0.5 s/deg.

3.2.2 2008 event

We continued by stacking the 2008 event, which was not studied before. In **Figure 14**, the top vespagram represents the whole event. We can clearly see the strong S and ScS arrivals, but also an intermediate SdS arrival. S arrives with a slowness of 3 s/deg and we can clearly see the SdS arrival, which arrives with an intermediate slowness of approximately 0.8



s/deg. Since the SdS arrival is visible in the linear vespagram, it is confirmed that it is a product of reflection within the lower mantle.

Since we wanted to further investigate

the area, we divided the region in two bins, a southern and a northern one and then produce their vespagrams (**Figure 14**,bottom).

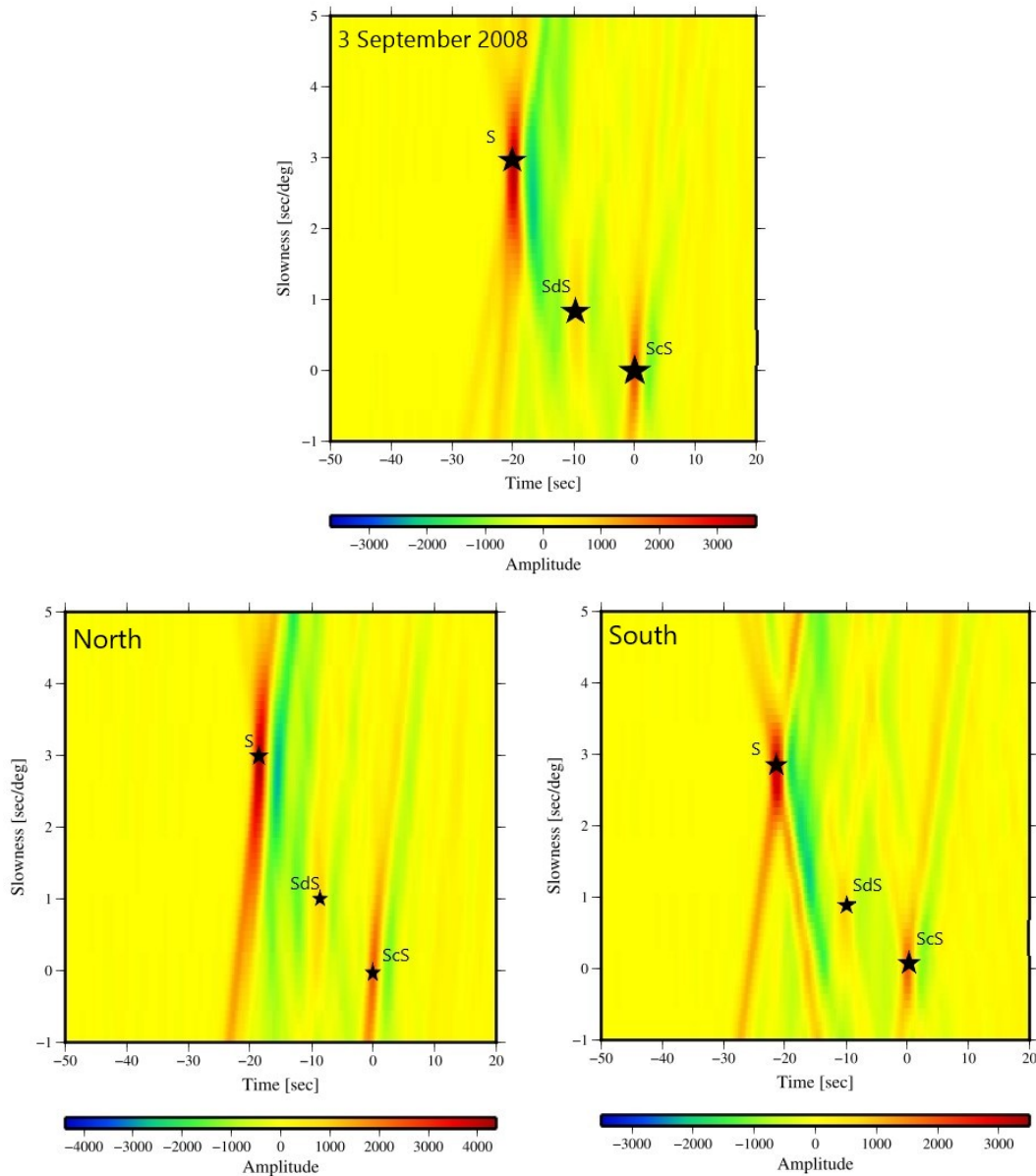


Figure 14: The top vespagram corresponds to the 2008, the bottom left to the north and the bottom right to the south bin of the study area, for the 2008 event. The maximum slownesses for the phases are depicted as stars.



In the northern bin, we can see a similar behavior like the complete 2008 event. The S phase arrives with a slowness of 3 s/deg, the SdS with a slowness of 0.8 s/deg and the ScS with a slowness of 0 s/deg. The amplitudes of the S phase in this bin have higher values, compared to the whole event. In the southern bin, the S and SdS phase appear to have lower values of amplitudes, therefore they are not that strong compared to the previous vespagrams. S arrives with a slowness of 3.3 s/deg, whereas the SdS phase arrives with a slowness of 0.9 s/deg.

Lastly, in the vespagram of the southern bin, we can see that the S phase

creates an red "X" from the slownesses. This appears to be a product of the S phase stacking and needed to be investigated more. It is especially important not to misinterpret the peaks from the "X" as SdS phases, because they are sidelobes from the stacked S arrival instead.

We started our interpretation of the SdS phase in terms of D" discontinuity depth by plotting three stacks, where each one corresponds to a different slowness value. This means that there is a stack with the maximum S, SdS and ScS slownesses, respectively. The first set of three (**Figure 15**), corresponds to the vespagram for the whole 2008 event.

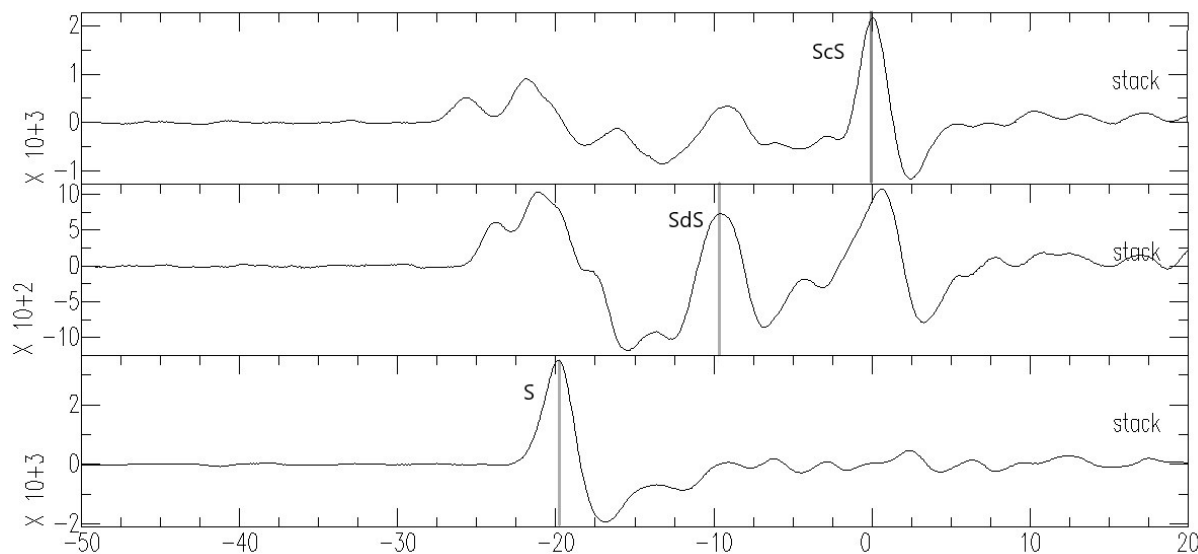


Figure 15: The stacks depict the S (bottom), SdS (middle) and ScS (top) maximum amplitudes, which correlate with the maximum slownesses. The S phase arrives with slowness of 3 s/deg, the SdS with a slowness of approximately 0.8 s/deg and the ScS with a slowness of 0 s/deg, for the 2008 event.



The top stack corresponds to a slowness of 0 s/deg, in which we can see the maximum ScS amplitude at 0 seconds. The second stack corresponds to a slowness of 0.8 s/deg in which the SdS phase arrives. Finally, the third stack corresponds to the maximum amplitude for the S arrival, which is at a slowness of 3 s/deg. For the 2008 event, the reference epicentral distance is 77.3471 degrees, therefore we concluded that the depth of the D'' discontinuity is equal to 2690km, equal to the depth obtained from the 2000 event.

We continued by plotting the southern and northern bins' stacks of the 2008 event.

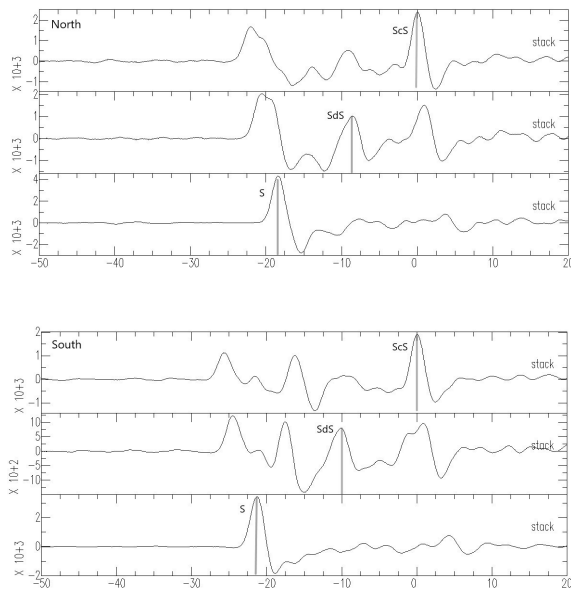


Figure 16: Set of stacks showing the maximum amplitude for each phase. The top three stacks correspond to the northern bin of the 2008 event, while the second set of stacks corresponds to the southern bin.

The top stacks of **Figure 16** are for the northern bin, while the bottom stacks for the southern bin. In the northern bin we do not observe any major differences

when comparing to the whole event stacks. In other words, there seems to be a great correlation with the complete event and one small detail we might is that the peaks appear to be more spiked in this case.

On the contrary, when we investigate the southern bin, we can see a different image compared to the whole event and the northern bin, based on the additional peak between the S and SdS. This can be explained if, at the same time, we look at the vespagram which corresponds to this set of stacks. Even though we see the maximum slowness of S at around 3 s/deg, we observe that there is an "X" created by the S slownesses, as mentioned before. This is just the result of the incoherent stacking of the S phase. It is very important to make sure we interpret the stacks correct and not confuse the S arrival and its products with the actual SdS arrival. Based on the vespagram, we observe that the maximum SdS slowness at 1 s/deg, corresponds to a specific time, therefore we could apply this to the stack and locate the actual SdS phase correctly.

When we look in more detail, there is a time difference between the arrival of the SdS phase between the northern and southern bin. For the northern bin, S arrives at approximately 8 seconds, whereas on the southern bin, S arrives at approximately 10 seconds ahead of ScS. Also, the SdS phase arrives earlier on the northern bin compared to the southern bin, as we can see from their stacks. Furthermore, in the southern bin, with a reference epicentral distance of 76.9784 degrees, we got a depth of 2700km for the discontinuity. On the contrary, when it comes to the northern bin, which has a reference epicentral



distance of 77.7665 degrees, the corresponding D" depth is equal to 2740km. We observe that the corresponding depth of the D" discontinuity varies when we divide the area in two latitudinal bins. Even though the depth for the event as a whole was equal to 2690km, when the study area was subdivided, we can see a different topography. Considering everything that has been analyzed above, we conclude that it was useful to divide the event in two bins, because we can see differences as well as extra observations, which were not visible when examining the event as a whole.

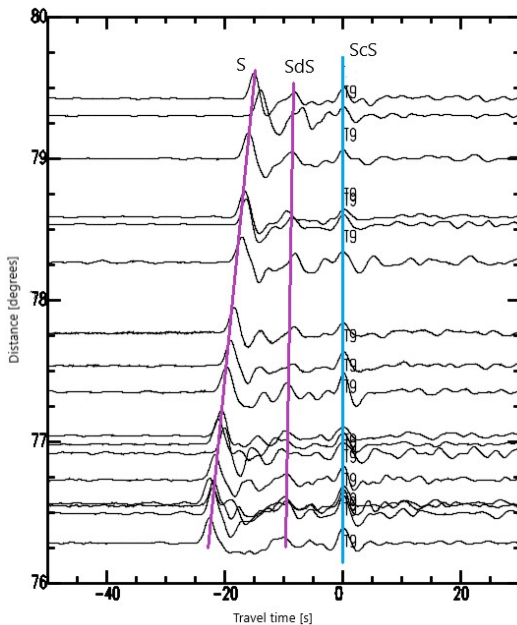


Figure 17: The seismograms of the 2008 event used for the vespagram process, plotted as a function of epicentral distance.

In **Figure 17** the seismograms used in the vespagram of the 2008 event are plotted as a function of epicentral distance. For the stacking we only used seismograms from stations with an epicen-

tral distance above 76 degrees. Moreover, we included seismograms which had very clear SdS and ScS phases and no noise. Even though one should normally include all the seismograms, we did not apply any filtering in the processing and this could lead to false results in the stacking.

Finally, we plotted the reflection points of those seismograms used for the stacking of 2008 on a map. In **Figure 18** we see three figures, where the top figure shows the reflection points of the whole event. The reflection points are color coded based on the depth was calculated with the use of the single seismogram method and therefore each point has an individual depth. From the map projection we can see that the dominant depth of the D" reflector for the 2008 event is approximately between 2700 and 2740km. Towards the north, we observe a couple of reflection points which reach 2800km, whereas towards the south we observe a couple of reflection depths which reach smaller depths of approximately 2650km. The two bottom figures correspond to the north and south bin map projections, respectively. In this case, the reflection points are color coded based on the depths calculated from each bin's stacks. Therefore, all the reflection points per bin have the same color.

In the map corresponding to the southern bin, two different groups of reflection points could be observed. The 10 reflection points on the map were separated in an eastern and western part, accordingly. Therefore, we subdivided the southern bin into two new bins: a western and eastern one, each containing 5 stations. The vespagrams for each bin are plotted in **Fig-**



Figure 19.

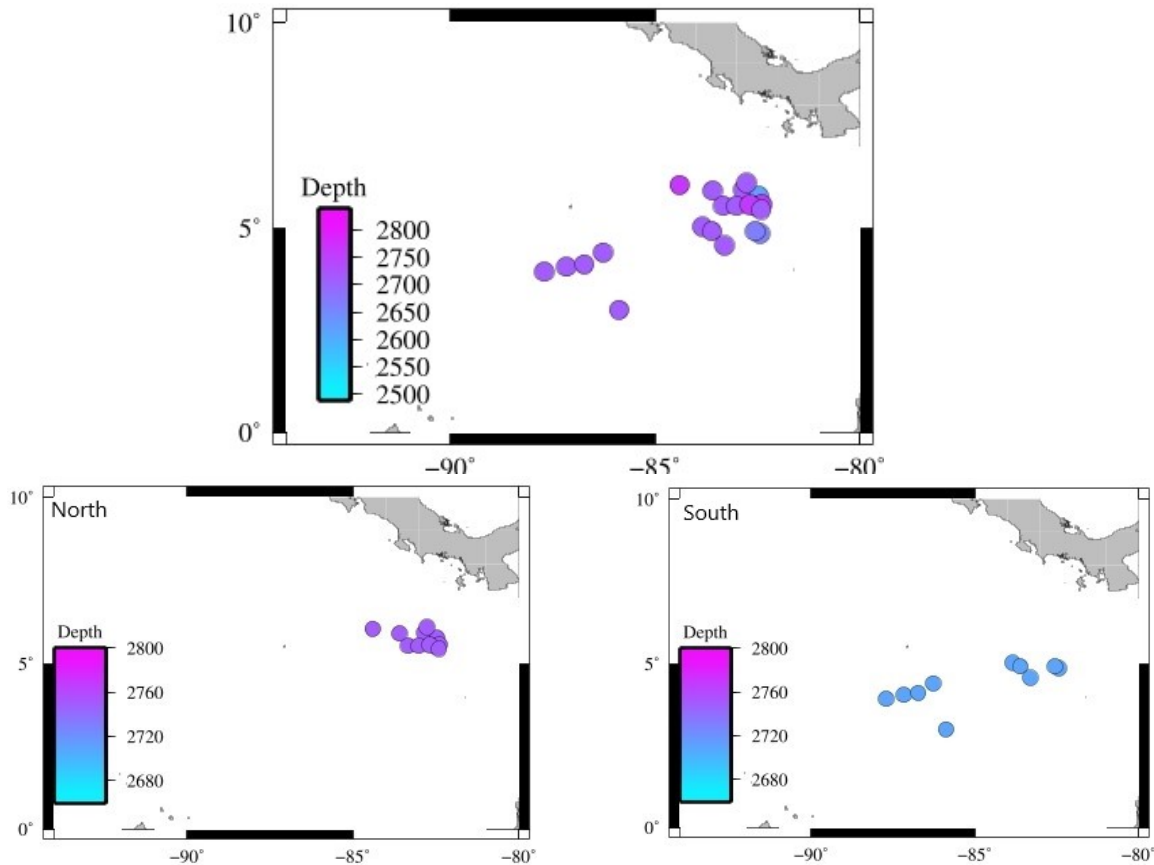


Figure 18: Map projections of the reflection depth for the 2008 event, calculated from single seismograms (top). The bottom left figure corresponds to the northern bin, while the bottom right corresponds to the southern bin and they are color coded based on the stack depth.

In both cases the SdS arrives with an intermediate slowness of around 0.9 sec/deg, compared to the two main phases. The SdS phase is more strong in the west bin, whereas in the east bin, SdS is more weakened and harder to observe. The ScS phase, on the other hand, is stronger on the eastern bin, whereas on the western bin we see that it is more weakened. In general, we can see that the western bin vespagram shows a slight "tilt" of the slownesses towards the west, whereas the eastern bin vespagram shows

the exact opposite. This could explain the resulting vespagram of the southern bin which seems to form an "X" with the S slownesses (**Figure 14**). The western bin has a reference epicentral distance of 78.5323 degrees and the resulting depth is 2690km. The eastern bin has a reference epicentral distance of 76.5589 degrees and the depth of the D" reflector is 2700km. If we compare it with the depth obtained from the stack of the southern bin as a whole, we see that the depths are approximately the same.

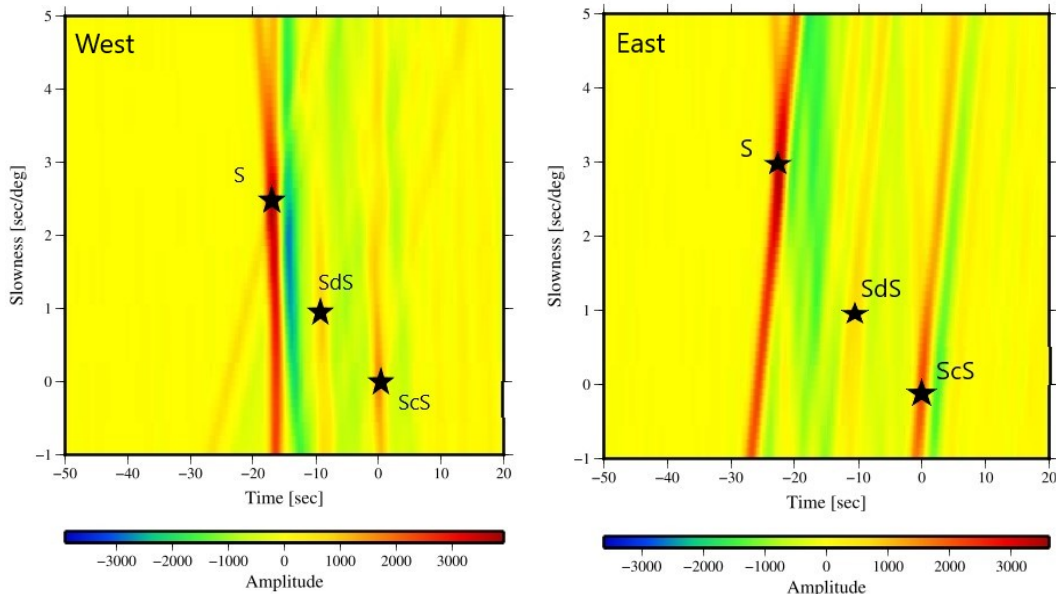


Figure 19: The subdivided southern bin’s vespagrams for the 2008 event. The left vespagram corresponds to the western bin and the right one to the eastern bin.

3.2.3 Amplitude Ratios

Based on the stacks that we have produced, we can calculate the maximum amplitude of the SdS phase and the ScS phase and get the amplitude ratio. The SdS/ScS amplitude ratio for the 2000 event, which was calculated from the stacks is 0.63, whereas the ratio for the 2008 event is 0.57. As far as the divided 2008 event is concerned, the SdS/ScS ratio for the north bin is equal to 0.59 while for the south bin it is 1. Lastly, the SdS/ScS ratio for the east bin is 0.41 and for the west bin is 0.8.

We repeated the same procedure for the single seismograms method in order to compare the amplitude ratios. Firstly, for the 2000 event, the amplitude ration of SdS/ScS is equal to 0.51. For the whole 2008 event, the SdS/ScS ratio is equal to 0.48, the north bin ratio is 0.59 and lastly the south bin is 0.57. The east bin has an amplitude ratio of 0.23, whereas the west

bin 0.72.

In general, it appears that the amplitude rations calculated from the single seismograms show smaller values compared to the amplitude ratios calculated from the stacking method. In order to be able to make conclusions from the amplitude ratios, more detailed research is required. We did not go any further on this topic, therefore no conclusions were made out of it.

3.3 Comparison with tomography

As a final step, we decided to correlate our results with a tomographic map. The tomographic models of seismic velocity variations are one of the main methods used in order to improve our understanding of the deep Earth structure. For this project we used the S20RTS



mantle model [Van Heijst et al., 1999], which gives shear wave velocity perturbations in the mantle. Additionally, we also used the S40RTS mantle model [Ritsema et al., 2011] in order to compare the results obtained by the two tomographic models. If the D" discontinuity topography and the shear wave velocity perturbations from the tomographic model have a common origin (like for example temperature variations) then we expect to find a correlation between the two. In order to run the models, a list of latitude and longitude values which covered the whole study area were used, in steps of 1 degree. Moreover, a constant depth of 2800km was chosen for the model, so that it would be above the CMB. After running the model, we created a contour map with the latitude, longitude and dV_s/V_s .

3.3.1 S20RTS

Since we wanted to combine and correlate the seismic velocities with the calculated D" discontinuity depth, we plotted the tomographic map along with the D" reflector depth map in the same figure (**Figure 20**).

We can observe that the reflection points from the events used in this study, are all located in a increased shear wave velocity region. More specifically, in the center of the study region the shear wave velocity is the largest, while it decreases towards the edges of the map and the north part.

Moreover, we wanted to get a better understanding of how the shear wave velocity changes as a function of latitude. Therefore, for a constant longitude of 85

degrees, we plotted dV_s/V_s as a function of latitude, in steps of 1 degree. This can be seen in **Figure 21**.

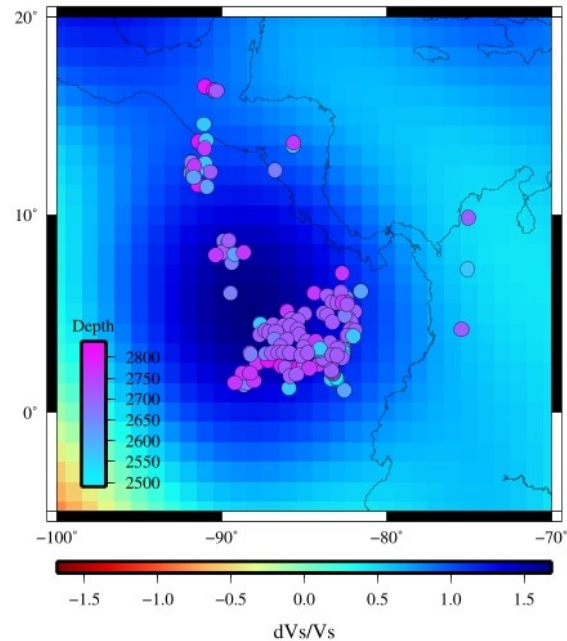


Figure 20: A tomographic map, using the S20RTS model, of the study area for a constant depth of 2800km. The circles represent the color-coded D" reflector depth.

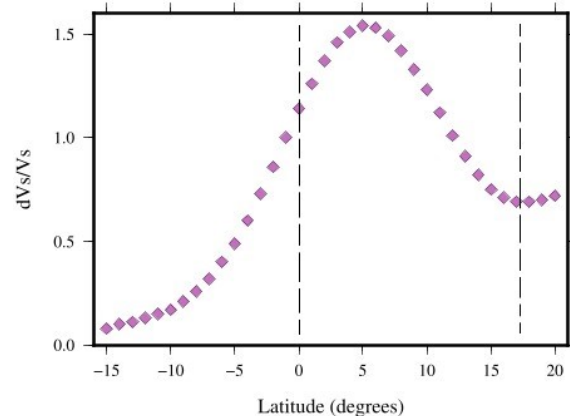


Figure 21: The variation of the shear wave velocity as a function of latitude, for a constant longitude of 85 degrees. The region where the reflection points are located, is closed within the dashed lines.



Indeed we observe that towards the center of the region, there is an increase in the shear wave velocity, reaching the maximum value at 5 degrees, while it reduces towards the edges. There is a greater decrease towards lower latitudes, whereas towards the north the reduction is smaller. The region where the reflection points are concentrated is marked with a box and is in the range between 0 and 17 degrees.

If we combine **Figure 21** with the bottom right of **Figure 11**, so that we compare them (**Figure 22**), then we can observe a correlation between them, but it appears to be a bit shifted.

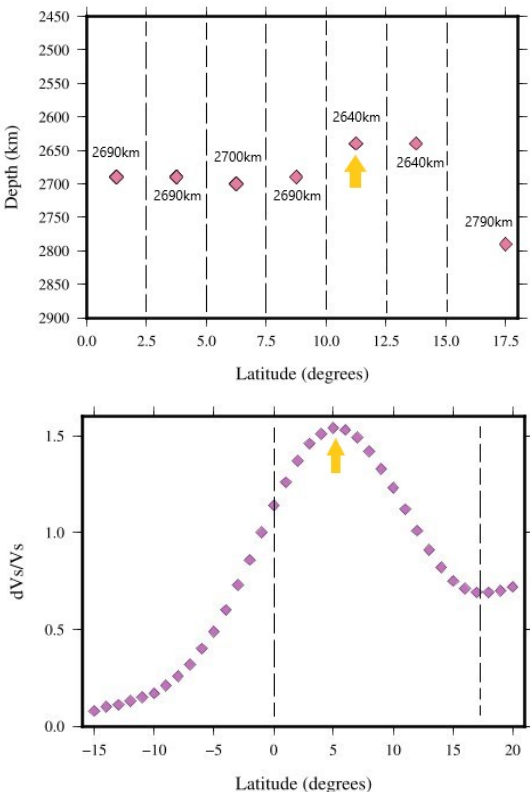


Figure 22: A combination of the modified Figures 11 and 21, for comparison purposes. The arrow marks the maximum peak for each plot.

More precisely, the peak on the dV_s/V_s plot is at approximately 5 degrees, whereas the peak at the depth plot is between 10 and 12.5 degrees. Apart from this shift, the results seem to correlate with each other.

Similar to **Figure 21**, now for a constant latitude of 4 degrees, we plotted the variation of dV_s/V_s as a function of longitude with 1 degree step. The lowest values of shear wave velocity are located towards the west and continuing towards the east we see an abrupt increase with the maximum velocity at approximately -88 degrees. After that point and moving even more towards the east, the velocity decreases again. We can see that the area where the reflection points are located is a region of high shear wave velocity, which is clear not only on the latitude but also on the longitude cross section.

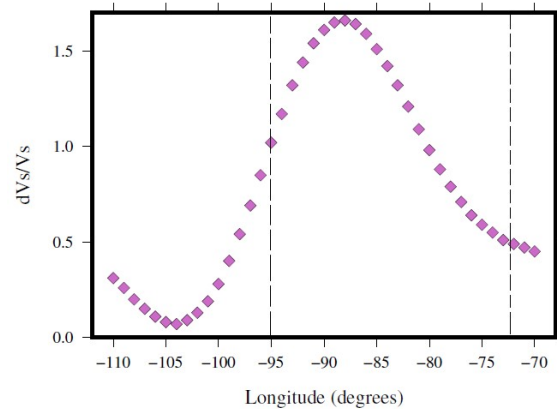


Figure 23: The variation of the shear wave velocity as a function of longitude, for a constant latitude of 4 degrees. The region where most of the reflection points are concentrated is closed within the dashed lines.

If we compare this figure, with **Figure 12** and combine them in **Figure 24** we observe that the reflection points of al-



3.3 Comparison with tomography

most constant depth, are all located in a high shear wave velocity region. The peak of the depth plot is located between -92.5 and -90 degrees, whereas the peak at the dV_s/V_s plot is at -88 degrees. Therefore the shift is smaller in this case, but it is still present.

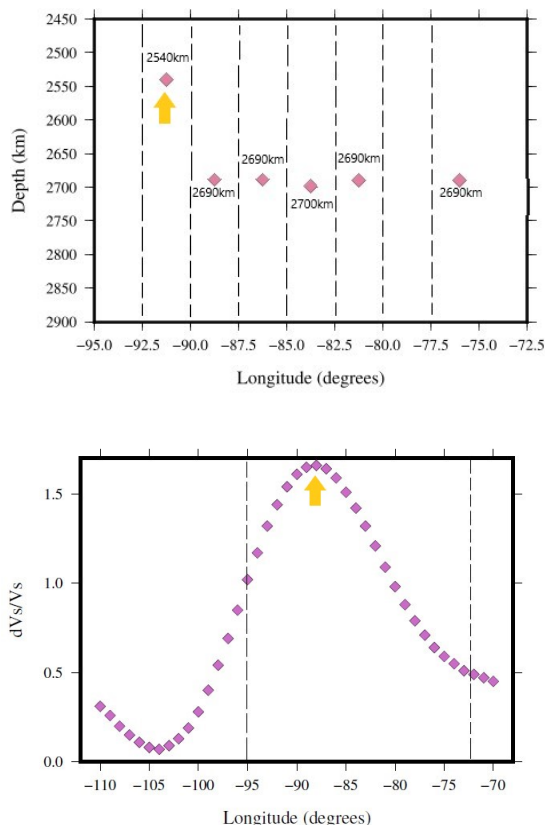


Figure 24: A combination of the modified Figures 12 and 23, for comparison purposes. The arrow marks the maximum peak for each plot.

3.3.2 S40RTS

Similarly, like in the S20RTS, we followed the exact same procedure for the S40RTS model and plotted the reflection points along with the tomographic map. The resulting map is depicted in **Figure 25**. Once again, it is obvious that most of the

reflection points are concentrated in an area of high shear wave velocity. In this case, the velocities appear to be of higher values reaching 2.5 and even beyond that. With the use of the S40RTS mantle model, which is more detailed compared to the S20RTS model, the velocity variations are greater.

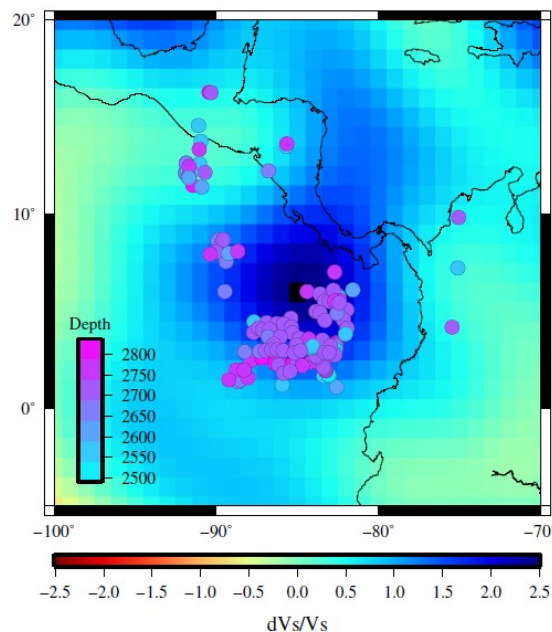


Figure 25: A tomographic map, using the S40RTS model, of the study area for a constant depth of 2800km. The circles represent the color coded D'' reflector depth.

Since we wanted to explore the variations of the shear wave velocity as a function of latitude and longitude, we plotted them in **Figure 26**. For the latitude plot, we chose a constant longitude of 85 degrees and for the longitude plot, we chose a constant latitude of 4 and both plots are in a step of 1 degree, similarly like we did on the S20RTS mantle model. From this plots, one can notice the difference in detail when it comes to the two mantle models. The dV_s/V_s variations as a function of



both latitude and longitude appear to be more robust and show a different image from the S20RTS model.

For comparison purposes, we combined **Figure 11, 12** and **Figure 26**. We once again observed a shift in the peaks and more specifically, the peak in the dV_s/V_s versus latitude plot is observed at approximately 6 degrees, whereas in the cor-

responding depth plot is at 10 degrees (**Figure 27**(top)). Respectively, on the longitude plots, the peak in the dV_s/V_s plot is at -85, whereas in the depth plot it is at -90 (**Figure 27**(bottom)). Even though the shift between the two peaks reduced in the latitude plot, in the longitude plot the shift became even greater.

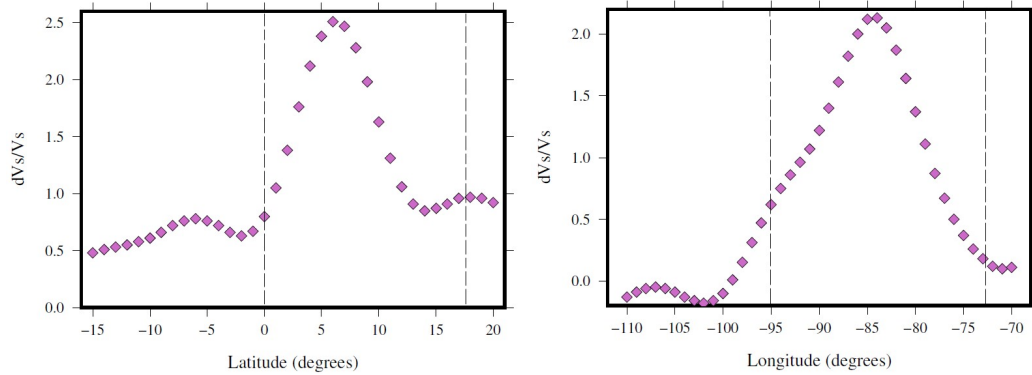


Figure 26: The variation of the shear wave velocity as a function of latitude and longitude.

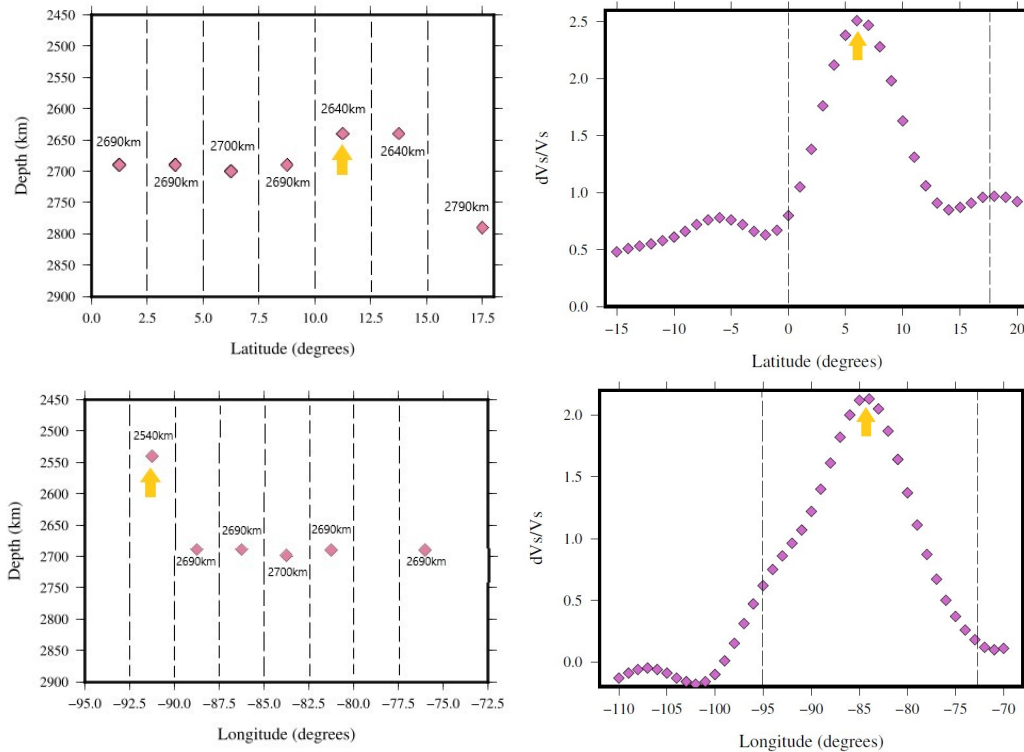


Figure 27: **Top:** Depth and dV_s/V_s latitude plots. **Bottom:** Depth and dV_s/V_s longitude plots.



4 Discussion

Throughout this study, we have analyzed a variety of events in order to image the D" reflector, above the CMB. We studied 12 events which were used in previous studies and extended the work, by searching for additional events. Apart from the 2008 event, which was an addition, three more events were processed but did not show any clear SdS arrival and that is why they were not included. Even though the majority of the events which were included in this study have already been studied, we followed a different processing procedure.

Firstly, the most important difference in the processing is the fact that we used single seismograms for observing SdS and determining D" discontinuity depth. All the previous studies have followed the stacking and migration methods. They used the Velocity Spectral Analysis (vespa) in order to magnify the SdS arrival and many of them also used n-th root vespagrams. It is not easy to observe the SdS arrival on single seismograms and it can be time consuming, but the averaging present when stacking, might remove details in the D" discontinuity topography that would be of interest. In the Results section, we determined the depth of the D" reflector using stacking and vespagrams and compared it with the depth calculated based on the single seismograms measurements. For our new 2008 event and using the single seismograms method, we observe that the dominant depth is approximately 2690-2700km, with a few reflection points at 2790km and 2640km. When calculating

the D" depth through the stacks, we get an average depth of 2690km for the whole event, which is different from the northern and southern bin. The results are similar, but the process of the single seismograms seems to be more detailed, since we get a depth for each reflection point, whereas from the stacking method we average per bin. The stacks show that the D" reflector seems to have a topography mostly from north to south, but from west to east as well, as it can be seen in **Figure 11** and **Figure 12**, respectively.

Apart from the 2008 event which was extensively analyzed here, we also need to consider the rest of the events which cover the study area. After using the time difference between SdS-ScS to make a correlation with topography of the D" reflector, we agree with all the previous studies that showed that there does not seem to be a constant depth for the discontinuity. As we can observe in **Figure 10**, the depth of the D" reflector varies between 2540km up until 2890km. In most cases, we can see that the dominant D" reflector depth is around 2690km. Moreover, we can observe smaller depths (approximately 2540km) towards the North, while in the South there seem to be some deeper reflectors, as well as some shallower. In the transition zone, between the northern and the southern region of the study area, a wide variety of depths can be observed, covering a range from 2500km up until 2800km. Our results seem to partially agree with [Thomas et al., 2004] who located shallower reflectors towards the north and deeper towards the south (see **Figure 11**). Since we used single seismograms for interpretation, we have a



wider depth variation and therefore more detailed, compared to other studies and that is why our results may vary.

In **Figure 20** and **Figure 25**, where we compare the tomographic maps of the S20RTS and S40RTS models, respectively, with the D" discontinuity reflection depths we see that most of the reflection points are located in a higher shear wave velocity region, if not the highest in the area of study. Based on **Figure 21**, **23** and **Figure 26** and assuming that temperature is associated with dV_s/V_s , while depth is associated with pressure, we can see a correlation between them. More specifically, higher temperatures correspond to lower values of dV_s/V_s , while the highest values of dV_s/V_s correspond to low temperatures. Therefore, at the point where we observe the peak on the dV_s/V_s plot (**Figure 22**, **24** and **Figure 27**), we would expect the lower temperatures and therefore the shallower depths, based on Figure 18 of [Hirose et al., 2007]. We observe this, but as mentioned before, there appears to be a shift, wider on the latitude plots and smaller on the longitude plots. Additionally, after the point where we observed the maximum peaks on each plot and considering the relationship with temperature mentioned above, we can see that there seems to be an agreement to the Clapeyron slope corresponding to the perovskite to post-perovskite phase transition. More precisely, after the maximum peaks, the temperature increases along with depth. But since there is a shift between the peaks of the two plots, there is something else which might be causing it.

With the use of the PREM model [Dziewonski and Anderson, 1981], we

converted the SdS arrival time to depth values calculated from the stacking process and individual seismogram picks. Using PREM, we convert the depth values with to the corresponding pressure values. For the resulting dominant depth of 2700km, the corresponding pressure is equal to approximately 125GPa. Knowing that the conditions above which post-perovskite is stable are 120GPa and 2500K and keeping in mind the agreement with the Clapeyron slope from [Hirose et al., 2007], we can conclude that there seems to be a connection with the discontinuity, but since there is a shift there are more reasons which could possibly explain the discontinuity.

We searched the Atlas of the Underworld [van der Meer et al., 2018] for the specific region and for a depth of 2700km, and we found that the Trans-American anomaly is observed there. It is located beneath the Cocos plate and above the Core-Mantle Boundary and has been detected by [Niu and Wen, 2001], [Thomas et al., 2004], [Hutko et al., 2006], [Kito et al., 2007], as well as other studies. This anomaly is caused by the subduction of the Farallon/Panthalassa slab that started taking place during the Permian. Two cross sections for two different mantle models can be seen in **Figure 28** by [van der Meer et al., 2018], along with a map projection. The presence of this slab could possibly explain why there seems to be a shift between the two plots in our results and there is no absolute correlation with the perovskite to post-perovskite phase transition and might be the reason behind the observed shift.

From the two cross sections and es-



pecially the bottom one, it is clear that the slab reaches depths of 2600-2700km. Those depths also correspond to the estimated discontinuity depth, based on our results. As mentioned in the Introduction, subducted slabs are a possible scenario which could cause the generation of the D" discontinuity.

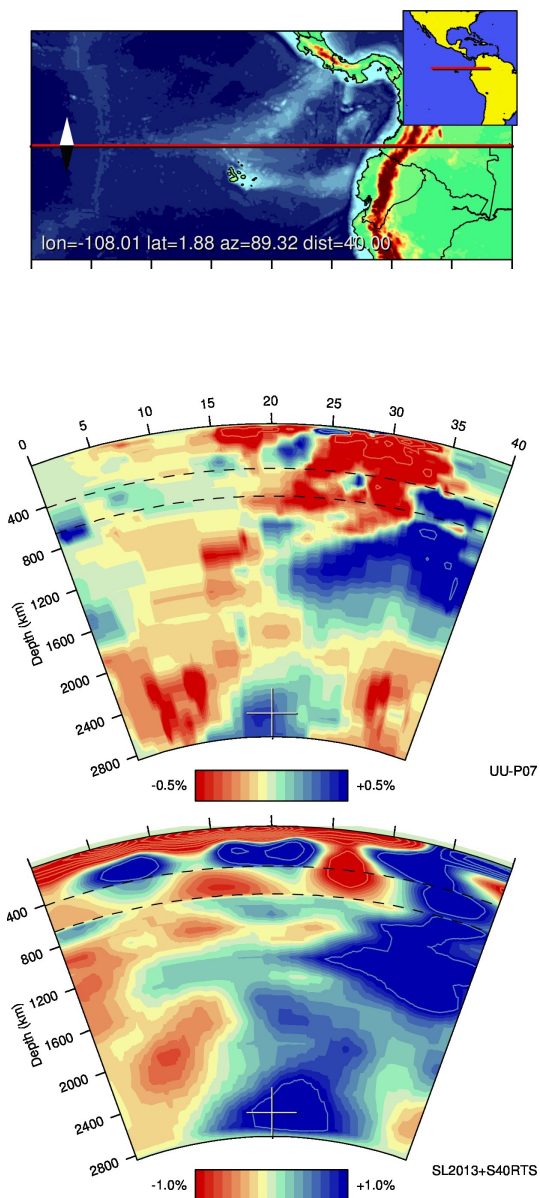


Figure 28: A map projection showing how the bottom two cross sections were produced [van der Meer et al., 2018]

[Thomas et al., 2004] also suggest the presence of a subducted slab, causing the generation of the discontinuity and further investigated this scenario. Of course, further research of the area is needed in order to be able to understand the generation of the discontinuity and associate it with one or more of the possible explanations.

5 Conclusions

We analyzed 16 South American earthquakes with the use of reflected shear waves in order to locate and image the D" discontinuity beneath the Cocos plate. We started the research with a use of a different method which is based on single seismograms and then we continued with the stacking method in order to compare the results obtained. The single seismogram method gave us a more detailed and localized image of the study region. The main advantage lies in the fact that each reflection point (off the D" discontinuity) corresponds to a separate depth. On the contrary, the stacking method, which was also applied in prior studies, requires for the division of the area in larger bins, each of them resulting in an average depth for the whole bin region. With the single seismogram approach, there is no averaging taking place and that is why the depth varies greatly between each point. We concluded that the dominant depth of the discontinuity seems to be between 2690 and 2700km, but it varies from 250 to 1000km above the CMB. The topography of the discontinuity appears to vary geographically as well, as we observed differences between the north and the south



region of the study area, as well as, the east and west. More precisely, the D" discontinuity deepens from north to south, in agreement with [Thomas et al., 2004]. Even though we relied on single seismograms for the interpretations, we also used the vespagram stacking process and compared the results. Based on the depths and the corresponding pressure values, we can see that there is a probable correlation between the discontinuity and the phase transition from perovskite to post-perovskite, since it takes place at similar depths and pressures, but it does not rely on it completely. The presence of the Trans-Americas anomaly at the region of this study, caused by the subduction of

the Farallon/Panthalassa slab could be a possible explanation of the shift observed in our results.

Since the results from the different methods agree, but not completely, we believe that it would be useful if both methods were used in future studies in order to compare the results obtained. Further research should be done concerning the imaging of the discontinuity with the use of different modeling methods, but most importantly multidisciplinary research is required in order to discover the nature and creation of the D" discontinuity and its interpretation in terms of the phase transition from perovskite to post-perovskite.

6 Acknowledgments

First of all, I would like to thank my supervisor, Dr. Arwen Deuss, for her guidance throughout my thesis. Our meetings were always helpful, not only for my project, but also on a personal level. Secondly, I would like to thank Michalis Koukias for helping me with building the Linux environment and helping me with any computer problems I was facing in the beginning of my project. Last but not least, I want to thank my family and friends (both from Utrecht and Greece) for the support throughout those months. Special thanks to my best friend Irini, my sister Emily, but also to Vasilis for bearing with me and my stress.



7 References

- [Akii and Richards, 2009] Akii, K. and Richards, P. G. (2009). Quantitative seismology. *University Science Books*.
- [Bullen, 1949] Bullen, K. E. (1949). Compressibility-pressure hypothesis and the earth's interior. *Geophys. J. Int.*, 5:335–368.
- [Cobden and Thomas, 2013] Cobden, L. and Thomas, C. (2013). The origin of d" reflections: a systematic study of seismic array data sets. *Geophys. J. Int.*, 194:1091–1118.
- [Crotwell et al., 1999] Crotwell, H. P., Owens, T. J., and Ritsema, J. (1999). The taup toolkit: Flexible seismic travel-time and ray-path utilities. *Seismological Research Letters*, 70:154–160.
- [Dahm, 1934] Dahm, C. (1934). A study of dilatational wave velocity in the earth as a function of depth, based on a comparison of the p, p" and pcp phases. *PhD dissertation. St. Luis University, St. Luis*.
- [Davies et al., 1971] Davies, D., Kelly, E. J., and Filson, J. R. (1971). Vespa process for analysis of seismic signals. *Nature Phys. Sci.*, 232:8–13.
- [Dziewonski and Anderson, 1981] Dziewonski, A. M. and Anderson, D. L. (1981). Preliminary reference earth model. *Physics of the Earth and Planetary Interiors*, 25:297–356.
- [Dziewonski et al., 1981] Dziewonski, A. M., Chou, T. A., and Woodhouse, J. H. (1981). Determination of earthquake source parameters from waveform data for studies of global and regional seismicity. *J. Geophys. Res.*, 86:2825–2852.
- [Helffrich et al., 2013] Helffrich, G., Wookey, J., and Bastow, I. (2013). The seismic analysis code: A primer and user's guide. *Cambridge University Press 40 W. 20 St. New York, NY, United States*.
- [Hirose et al., 2007] Hirose, K., Wookey, J., and Bastow, I. (2007). Discovery of post-perovskite phase transition and the nature of d" layer. *Post-Perovskite: The Last Mantle Phase Transition*, pages 19–35.
- [Hutko et al., 2006] Hutko, A. R., Lay, T., Garnero, E. J., and Revenaugh, J. (2006). Seismic detection of folded subducted lithosphere at the core-mantle boundary. *Nature*, 441:333–336.
- [Kendall and Nangini, 1996] Kendall, J. M. and Nangini, C. (1996). Lateral variations in d" below the caribbean. *Geophysical Research Letters*, 23:399–402.



- [Kennett et al., 1995] Kennett, B. L. N., Engdahl, E. R., and Buland, R. (1995). Constraints on seismic velocities in the earth from traveltimes. *Geophys. J. Int.*, 122:108–124.
- [Kito et al., 2007] Kito, T., Rost, S., Thomas, C., and Garnero, E. J. (2007). New insights into the p- and s-wave velocity structure of the d" discontinuity beneath the cocos plate. *Geophysical Journal International*, 169:631–645.
- [Lay, 2008] Lay, T. (2008). Sharpness of the d" discontinuity beneath the cocos plate: Implications for the perovskite to post-perovskite phase transition. *Geophysical Research Letters*, 35.
- [Lay and Garnero, 2011] Lay, T. and Garnero, E. J. (2011). Deep mantle seismic modeling and imaging. *Annu. Rev. Earth Planet.*, 39:91–123.
- [Lay et al., 2004] Lay, T., Garnero, E. J., and Russell, S. A. (2004). Lateral variation of the d" discontinuity beneath the cocos plate. *Geophys. Res. Lett.*
- [Lay and Helmberger, 1983] Lay, T. and Helmberger, D. V. (1983). A lower mantle s-wave triplication and the shear velocity structure of d". *Geophysical Journal International*, 75:799–837.
- [Lay et al., 1998] Lay, T., Williams, Q., and Garnero, E. J. (1998). The core-mantle boundary layer and deep earth dynamics. *Nature*, 392.
- [Muirhead and Datt, 1976] Muirhead, K. J. and Datt, R. (1976). The n-th root process applied to seismic array data. *Geophysical Journal International*, 47:197–210.
- [Niu and Wen, 2001] Niu, F. and Wen, L. (2001). Strong seismic scatterers near the core-mantle boundary west of mexico. *Geophysical Research Letters*, 28:3557–3560.
- [Ritsema et al., 2011] Ritsema, J., Deuss, A., van Heijst, H. J., and Woodhouse, J. H. (2011). S40rts: a degree-40 shear-velocity model for the mantle from new rayleigh wave dispersion, teleseismic traveltime and normal-mode splitting function measurements. *Geophysical Journal International*, 184:1223–1236.
- [Stackhouse and Brodholt, 2007] Stackhouse, S. and Brodholt, J. P. (2007). High-temperature elasticity of mgsio₃ post-perovskite. *Post-Perovskite: The Last Mantle Phase Transition*.
- [Thomas et al., 2004] Thomas, C., Garnero, E. J., and Lay, T. (2004). High-resolution imaging of lowermost mantle structure under the cocos plate. *Journal of Geophysical Research*, 109.



-
- [van der Meer et al., 2018] van der Meer, D. G., van Hinsbergen, D. J. J., and Spakman, W. (2018). Atlas of the underworld: Slab remnants in the mantle, their sinking history, and a new outlook on lower mantle viscosity. *Tectonophysics*, 723:309–448.
- [Van Heijst et al., 1999] Van Heijst, H. J., Ritsema, J., and Woodhouse, J. H. (1999). *Eos(spring suppl.)*.
- [Weber, 1993] Weber, M. (1993). P- and s-wave reflections from anomalies in the lowermost mantle. *Geophys. J. Int.*, 115:183–210.
- [Wentzovitch et al., 2006] Wentzovitch, R. M., Tsychiya, T., and Tsuchiya, J. (2006). Mgsio(3) postperovskite at d" conditions. *Proc. Natl. Acad. Sci. USA*, 103:543–546.
- [Whittaker et al., 2015] Whittaker, S., Thorne, M. S., Schmerr, N. C., and Miyagi, L. (2015). Seismic array constraints on the d" discontinuity beneath central america. *J. Geophys. Res. Solid Earth*, 121:152–169.
- [Wookey et al., 2005] Wookey, J., Stackhouse, S., Kendall, J. M., Brodholt, J., and Price, G. D. (2005). Efficacy of the post-perovskite phase as an explanation for lowermost-mantle seismic properties. *Nature*, 438:1004–1007.
- [Wyssession et al., 1998] Wyssession, M. E., Lay, T., Revenaugh, J., Williams, Q., Garnero, E. J., Jeanloz, R., and Kellogg, L. H. (1998). The d" discontinuity and its implications. *The Core-Mantle Boundary Region, Geodyn. Ser.*, 28.



8 Appendix

Tables Used for D" reflector depth correlation.

Event at the CMB

Distance (deg)	Depth (km)	Phase Name	Travel Time (s)	Ray Param p (s/deg)	Takeoff (deg)	Incident (deg)	Purist Name
36.61	2889.0	p	354.64	4.280	-74.18	12.90	36.61 = p
36.61	2889.0	PcP	354.74	4.271	73.76	12.87	36.61 = PcP
36.61	2889.0	SKS	650.28	7.577	65.19	13.64	36.61 = SKS
36.61	2889.0	s	651.16	7.993	-73.24	14.40	36.61 = s
36.61	2889.0	ScS	651.36	7.977	72.87	14.37	36.61 = ScS
36.61	2889.0	PKIKP	755.76	0.888	11.52	2.66	36.61 = PKIKP
36.61	2889.0	SKIKS	968.97	0.939	6.46	1.67	36.61 = SKIKS

Event at the D"

Distance (deg)	Depth (km)	Phase Name	Travel Time (s)	Ray Param p (s/deg)	Takeoff (deg)	Incident (deg)	Purist Name
36.61	2700.0	p	351.43	4.622	-78.90	13.95	36.61 = p
36.61	2700.0	PcP	360.48	4.040	59.06	12.17	36.61 = PcP
36.61	2700.0	s	644.45	8.624	-76.72	15.57	36.61 = s
36.61	2700.0	ScS	662.51	7.539	58.30	13.57	36.61 = ScS
36.61	2700.0	PKIKP	769.34	0.875	10.71	2.62	36.61 = PKIKP
36.61	2700.0	SKIKS	994.85	0.931	6.03	1.66	36.61 = SKIKS

36.61	2839.0	p	353.67	4.368	-75.39	13.17	36.61 = p
36.61	2839.0	PcP	355.93	4.199	68.46	12.65	36.61 = PcP
36.61	2839.0	s	649.23	8.158	-74.18	14.70	36.61 = s
36.61	2839.0	SKS	653.26	7.585	63.45	13.65	36.61 = SKS
36.61	2839.0	ScS	653.70	7.837	67.57	14.12	36.61 = ScS
36.61	2839.0	PKIKP	759.35	0.885	11.30	2.64	36.61 = PKIKP
36.61	2839.0	SKIKS	975.80	0.937	6.34	1.67	36.61 = SKIKS

36.61	2789.0	p	352.79	4.457	-76.72	13.44	36.61 = p
36.61	2789.0	PcP	357.39	4.137	64.61	12.46	36.61 = PcP
36.61	2789.0	s	647.41	8.324	-75.14	15.01	36.61 = s
36.61	2789.0	SKS	656.43	7.589	61.79	13.66	36.61 = SKS
36.61	2789.0	ScS	656.55	7.720	63.70	13.90	36.61 = ScS
36.61	2789.0	PKIKP	762.94	0.881	11.09	2.63	36.61 = PKIKP
36.61	2789.0	SKIKS	982.64	0.935	6.23	1.67	36.61 = SKIKS

36.61	2739.0	p	352.00	4.548	-78.31	13.72	36.61 = p
36.61	2739.0	PcP	359.06	4.081	61.47	12.29	36.61 = PcP
36.61	2739.0	s	645.71	8.491	-76.16	15.32	36.61 = s
36.61	2739.0	SKS	659.77	7.591	60.22	13.66	36.61 = SKS
36.61	2739.0	ScS	659.78	7.615	60.54	13.71	36.61 = ScS
36.61	2739.0	PKIKP	766.53	0.878	10.89	2.62	36.61 = PKIKP
36.61	2739.0	SKIKS	989.49	0.933	6.12	1.66	36.61 = SKIKS

36.61	2689.0	p	351.28	4.643	-79.07	14.02	36.61 = p
36.61	2689.0	PcP	360.90	4.029	58.43	12.13	36.61 = PcP
36.61	2689.0	s	644.12	8.660	-76.83	15.63	36.61 = s
36.61	2689.0	ScS	663.32	7.519	57.71	13.53	36.61 = ScS
36.61	2689.0	PKIKP	770.13	0.875	10.66	2.61	36.61 = PKIKP
36.61	2689.0	SKIKS	996.36	0.931	6.01	1.66	36.61 = SKIKS

36.61	2639.0	p	350.63	4.734	-79.51	14.29	36.61 = p
36.61	2639.0	PcP	362.91	3.981	55.79	11.99	36.61 = PcP
36.61	2639.0	s	642.98	8.834	-77.66	15.96	36.61 = s
36.61	2639.0	ScS	667.16	7.429	55.23	13.37	36.61 = ScS
36.61	2639.0	PKIKP	773.76	0.871	10.43	2.61	36.61 = PKIKP
36.61	2639.0	SKIKS	1003.25	0.929	5.90	1.66	36.61 = SKIKS

36.61	2589.0	p	349.99	4.830	-80.32	14.59	36.61 = p
36.61	2589.0	PcP	365.04	3.938	53.48	11.85	36.61 = PcP
36.61	2589.0	s	641.15	9.005	-78.37	16.27	36.61 = s
36.61	2589.0	ScS	671.23	7.345	53.03	13.21	36.61 = ScS
36.61	2589.0	PKIKP	777.40	0.868	10.71	2.60	36.61 = PKIKP
36.61	2589.0	SKIKS	1010.17	0.927	5.79	1.65	36.61 = SKIKS

36.61	2539.0	p	349.41	4.927	-81.14	14.89	36.61 = p
36.61	2539.0	PcP	367.32	3.896	51.37	11.72	36.61 = PcP
36.61	2539.0	s	639.78	9.178	-79.18	16.59	36.61 = s
36.61	2539.0	ScS	675.52	7.266	51.04	13.07	36.61 = ScS
36.61	2539.0	PKIKP	781.06	0.865	9.99	2.59	36.61 = PKIKP
36.61	2539.0	SKIKS	1017.11	0.926	5.68	1.65	36.61 = SKIKS

Deg73.5

Distance (deg)	Depth (km)	Phase Name	Travel Time (s)	Ray Param p (s/deg)	Takeoff (deg)	Incident (deg)	Purist Name
38.00	2889.0	p	360.59	4.319	-76.13	13.02	38.00 = p
38.00	2889.0	PcP	360.68	4.310	75.67	12.99	38.00 = PcP
38.00	2889.0	SKS	660.77	7.567	65.03	13.62	38.00 = SKS
38.00	2889.0	s	662.28	8.070	-75.20	14.54	38.00 = s
38.00	2889.0	ScS	662.46	8.054	74.78	14.51	38.00 = ScS
38.00	2889.0	PKIKP	757.00	0.919	11.92	2.75	38.00 = PKIKP
38.00	2889.0	SKIKS	970.29	0.971	6.68	1.73	38.00 = SKIKS

38.00	2700.0	p	357.87	4.649	-80.75	14.03	38.00 = p
38.00	2700.0	PcP	366.11	4.091	60.27	12.32	38.00 = PcP
38.00	2700.0	s	656.46	8.688	-78.66	15.68	38.00 = s
38.00	2700.0	SKS	673.01	7.590	58.93	13.66	38.00 = SKS
38.00	2700.0	ScS	673.03	7.637	59.53	13.75	38.00 = ScS
38.00	2700.0	PKIKP	770.58	0.905	11.08	2.71	38.00 = PKIKP
38.00	2700.0	SKIKS	996.16	0.963	6.24	1.72	38.00 = SKIKS

38.00	2839.0	p	359.75	4.404	-77.32	13.28	38.00 = p
38.00	2839.0	PcP	361.78	4.240	69.95	12.78	38.00 = PcP
38.00	2839.0	s	660.58	8.232	-76.13	14.84	38.00 = s
38.00	2839.0	SKS	663.76	7.578	63.35	13.64	38.00 = SKS
38.00	2839.0	ScS	664.62	7.920	69.08	14.27	38.00 = ScS
38.00	2839.0	PKIKP	760.59	0.915	11.70	2.74	38.00 = PKIKP
38.00	2839.0	SKIKS	977.11	0.969	6.56	1.73	38.00 = SKIKS

38.00	2789.0	p	359.00	4.488	-78.55	13.54	38.00 = p
38.00	2789.0	PcP	363.15	4.182	65.96	12.60	38.00 = PcP
38.00	2789.0	s	659.00	8.392	-77.03	15.14	38.00 = s
38.00	2789.0	SKS	666.93	7.585	61.74	13.65	38.00 = SKS
38.00	2789.0	ScS	667.31	7.809	65.06	14.06	38.00 = ScS
38.00	2789.0	PKIKP	764.18	0.912	11.48	2.73	38.00 = PKIKP
38.00	2789.0	SKIKS	983.95	0.967	6.44	1.72	38.00 = SKIKS

38.00	2739.0	p	358.32	4.579	-80.39	13.82	38.00 = p
38.00	2739.0	PcP	364.74	4.129	62.76	12.44	38.00 = PcP
38.00	2739.0	s	657.52	8.559	-78.15	15.45	38.00 = s
38.00	2739.0	SKS	670.28	7.589	60.21	13.66	38.00 = SKS
38.00	2739.0	ScS	670.39	7.709	61.83	13.88	38.00 = ScS
38.00	2739.0	PKIKP	767.77	0.908	11.27	2.71	38.00 = PKIKP
38.00	2739.0	SKIKS	990.80	0.965	6.33	1.72	38.00 = SKIKS

38.00	2689.0	p	357.75	4.668	-80.80	14.09	38.00 = p
38.00	2689.0	PcP	366.51	4.080	59.64	12.29	38.00 = PcP
38.00	2689.0	s	656.14	8.728	-78.92	15.76	38.00 = s
38.00	2689.0	SKS	673.80	7.591	58.59	13.66	38.00 = SKS
38.00	2689.0	ScS	673.81	7.618	58.92	13.71	38.00 = ScS
38.00	2689.0	PKIKP	771.37	0.905	11.03	2.70	38.00 = PKIKP
38.00	2689.0	SKIKS	997.67	0.963	6.21	1.72	38.00 = SKIKS

38.00	2639.0	p	357.25	4.752	-80.76	14.35	38.00 = p
38.00	2639.0	PcP	368.46	4.035	56.95	12.15	38.00 = PcP
38.00	2639.0	s	654.86	8.896	-79.64	16.07	38.00 = s
38.00	2639.0	ScS	677.51	7.533	56.41	13.56	38.00 = ScS
38.00	2639.0	PKIKP	775.00	0.901	10.79	2.70	38.00 = PKIKP
38.00	2639.0	SKIKS	1004.56	0.961	6.10	1.71	38.00 = SKIKS

38.00	2589.0	p	356.73	4.849	-81.71	14.65	38.00 = p
38.00	2589.0	PcP	370.54	3.993	54.57	12.02	38.00 = PcP
38.00	2589.0	s	653.66	9.063	-80.32	16.38	38.00 = s
38.00	2589.0	ScS	681.47	7.453	54.16	13.41	38.00 = ScS
38.00	2589.0	PKIKP	778.64	0.898	10.56	2.69	38.00 = PKIKP
38.00	2589.0	SKIKS	1011.48	0.959	5.99	1.71	38.00 = SKIKS

38.00	2539.0	p	356.24	4.952	-83.26	14.97	38.00 = p
38.00	2539.0	PcP	372.75	3.953	52.45	11.90	38.00 = PcP
38.00	2539.0	s	652.59	9.233	-81.16	16.70	38.00 = s
38.00	2539.0	ScS	685.67	7.376	52.13	13.27	38.00 = ScS
38.00	2539.0	PKIKP	782.29	0.895	10.34	2.68	38.00 = PKIKP
38.00	2539.0	SKIKS	1018.42	0.957	5.88	1.71	38.00 = SKIKS

13.42

3.86

7.5

10.9

14.08

17.16

20.02

22.76

11.64

3.4

6.56

9.52

12.28

14.84

17.24

19.5



Deg74.3

Distance (deg)	Depth (km)	Phase Name	Travel Time (s)	Rav p (s/deg)	Param (deg)	Takeoff (deg)	Incident Distance (deg)	Purist Name
38.39 2889.0	p		362.30	4.329	-76.64	13.05	38.39	= p
38.39 2889.0	PcP		362.38	4.321	76.21	13.07	38.39	= PcP
38.39 2889.0	SKS		663.75	7.564	64.98	13.61	38.39	= SKS
38.39 2889.0	s		665.47	8.090	-75.75	14.58	38.39	= s
38.39 2889.0	ScS		665.64	8.074	75.31	14.55	38.39	= ScS
38.39 2889.0	PKIKP		757.37	0.928	12.04	2.77	38.39	= PKIKP
38.39 2889.0	SKIKS		970.68	0.980	6.74	1.75	38.39	= SKIKS

38.39 2700.0	p		359.72	4.655	-81.16	14.05	38.39	= p
38.39 2700.0	PcP		367.73	4.104	60.61	12.36	38.39	= PcP
38.39 2700.0	s		659.88	8.706	-79.27	15.72	38.39	= s
38.39 2700.0	SKS		676.01	7.590	58.93	13.66	38.39	= SKS
38.39 2700.0	ScS		676.05	7.664	59.87	13.80	38.39	= ScS
38.39 2700.0	PKIKP		770.93	0.914	11.19	2.73	38.39	= PKIKP
38.39 2700.0	SKIKS		996.54	0.972	6.30	1.73	38.39	= SKIKS

38.39 2839.0	p		361.49	4.413	-77.86	13.31	38.39	= p
38.39 2839.0	PcP		363.46	4.250	70.32	12.81	38.39	= PcP
38.39 2839.0	s		663.83	8.251	-76.67	14.88	38.39	= s
38.39 2839.0	SKS		666.75	7.576	63.32	13.64	38.39	= SKS
38.39 2839.0	ScS		667.75	7.941	69.49	14.31	38.39	= ScS
38.39 2839.0	PKIKP		760.94	0.924	11.81	2.76	38.39	= PKIKP
38.39 2839.0	SKIKS		977.51	0.978	6.62	1.74	38.39	= SKIKS

38.39 2789.0	p		360.77	4.497	-79.11	13.56	38.39	= p
38.39 2789.0	PcP		364.80	4.194	66.34	12.64	38.39	= PcP
38.39 2789.0	s		662.32	8.411	-77.60	15.17	38.39	= s
38.39 2789.0	SKS		669.93	7.584	61.72	13.65	38.39	= SKS
38.39 2789.0	ScS		670.39	7.833	65.44	14.11	38.39	= ScS
38.39 2789.0	PKIKP		764.53	0.920	11.59	2.75	38.39	= PKIKP
38.39 2789.0	SKIKS		984.34	0.975	6.50	1.74	38.39	= SKIKS

38.39 2739.0	p		360.13	4.586	-80.92	13.84	38.39	= p
38.39 2739.0	PcP		366.38	4.142	63.10	12.48	38.39	= PcP
38.39 2739.0	s		660.89	8.577	-78.75	15.48	38.39	= s
38.39 2739.0	SKS		673.28	7.589	60.20	13.66	38.39	= SKS
38.39 2739.0	ScS		673.44	7.734	62.18	13.93	38.39	= ScS
38.39 2739.0	PKIKP		768.12	0.917	11.38	2.74	38.39	= PKIKP
38.39 2739.0	SKIKS		991.19	0.973	6.39	1.74	38.39	= SKIKS

38.39 2689.0	p		359.60	4.675	-81.35	14.12	38.39	= p
38.39 2689.0	PcP		368.13	4.094	59.96	12.33	38.39	= PcP
38.39 2689.0	s		659.59	8.744	-79.47	15.79	38.39	= s
38.39 2689.0	SKS		676.80	7.590	58.58	13.66	38.39	= SKS
38.39 2689.0	ScS		676.82	7.644	59.26	13.76	38.39	= ScS
38.39 2689.0	PKIKP		771.73	0.913	11.14	2.73	38.39	= PKIKP
38.39 2689.0	SKIKS		998.05	0.971	6.27	1.73	38.39	= SKIKS

38.39 2639.0	p		359.14	4.757	-81.15	14.37	38.39	= p
38.39 2639.0	PcP		370.05	4.050	57.27	12.19	38.39	= PcP
38.39 2639.0	s		658.38	8.910	-80.13	16.10	38.39	= s
38.39 2639.0	ScS		680.49	7.561	56.73	13.61	38.39	= ScS
38.39 2639.0	PKIKP		775.35	0.910	10.90	2.72	38.39	= PKIKP
38.39 2639.0	SKIKS		1004.94	0.970	6.15	1.73	38.39	= SKIKS

38.39 2589.0	p		358.66	4.854	-82.16	14.67	38.39	= p
38.39 2589.0	PcP		372.12	4.008	54.89	12.07	38.39	= PcP
38.39 2589.0	s		657.25	9.077	-80.83	16.41	38.39	= s
38.39 2589.0	ScS		684.42	7.482	54.47	13.46	38.39	= ScS
38.39 2589.0	PKIKP		778.29	0.907	10.67	2.71	38.39	= PKIKP
38.39 2589.0	SKIKS		1011.85	0.968	6.04	1.73	38.39	= SKIKS

38.39 2539.0	p		358.20	4.957	-83.70	14.98	38.39	= p
38.39 2539.0	PcP		374.32	3.968	52.73	11.95	38.39	= PcP
38.39 2539.0	s		656.20	9.244	-81.57	16.72	38.39	= s
38.39 2539.0	ScS		688.59	7.406	52.43	13.32	38.39	= ScS
38.39 2539.0	PKIKP		782.65	0.904	10.44	2.70	38.39	= PKIKP
38.39 2539.0	SKIKS		1018.79	0.966	5.93	1.72	38.39	= SKIKS

Deg75

Distance (deg)	Depth (km)	Phase Name	Travel Time (s)	Rav p (s/deg)	Param (deg)	Takeoff (deg)	Incident Distance (deg)	Purist Name
38.86 2889.0	p		364.33	4.340	-77.27	13.08	38.86	= p
38.86 2889.0	PcP		364.41	4.331	76.79	13.06	38.86	= PcP
38.86 2889.0	SKS		667.29	7.560	64.92	13.61	38.86	= SKS
38.86 2889.0	s		669.26	8.113	-76.38	14.62	38.86	= s
38.86 2889.0	ScS		669.42	8.097	75.94	14.59	38.86	= ScS
38.86 2889.0	PKIKP		757.81	0.938	12.17	2.80	38.86	= PKIKP
38.86 2889.0	SKIKS		971.15	0.990	6.81	1.77	38.86	= SKIKS

38.86 2700.0	p		361.90	4.661	-81.68	14.07	38.86	= p
38.86 2700.0	PcP		369.65	4.120	61.00	12.41	38.86	= PcP
38.86 2700.0	s		663.95	8.726	-79.97	15.75	38.86	= s
38.86 2700.0	SKS		679.55	7.589	58.92	13.66	38.86	= SKS
38.86 2700.0	ScS		679.64	7.694	60.75	13.85	38.86	= ScS
38.86 2700.0	PKIKP		771.36	0.924	11.32	2.76	38.86	= PKIKP
38.86 2700.0	SKIKS		997.01	0.982	6.37	1.75	38.86	= SKIKS

38.86 2839.0	p		363.55	4.423	-78.49	13.34	38.86	= p
38.86 2839.0	PcP		365.45	4.262	70.78	12.85	38.86	= PcP
38.86 2839.0	s		667.69	8.272	-77.32	14.92	38.86	= s
38.86 2839.0	SKS		670.30	7.574	63.28	13.63	38.86	= SKS
38.86 2839.0	ScS		671.46	7.967	69.99	14.35	38.86	= ScS
38.86 2839.0	PKIKP		761.39	0.934	11.94	2.79	38.86	= PKIKP
38.86 2839.0	SKIKS		977.97	0.988	6.69	1.76	38.86	= SKIKS

38.86 2789.0	p		362.87	4.507	-79.80	13.60	38.86	= p
38.86 2789.0	PcP		366.77	4.207	66.75	12.68	38.86	= PcP
38.86 2789.0	s		666.24	8.433	-78.30	15.21	38.86	= s
38.86 2789.0	SKS		673.48	7.582	61.70	13.65	38.86	= SKS
38.86 2789.0	ScS		674.06	7.859	65.87	14.16	38.86	= ScS
38.86 2789.0	PKIKP		764.97	0.930	11.72	2.78	38.86	= PKIKP
38.86 2789.0	SKIKS		984.81	0.986	6.57	1.76	38.86	= SKIKS

38.86 2739.0	p		362.28	4.594	-81.54	13.86	38.86	= p
38.86 2739.0	PcP		368.31	4.157	63.51	12.52	38.86	= PcP
38.86 2739.0	s		664.91	8.596	-79.40	15.51	38.86	= s
38.86 2739.0	SKS		676.82	7.587	60.18	13.66	38.86	= SKS
38.86 2739.0	ScS		677.06	7.763	62.59	13.98	38.86	= ScS
38.86 2739.0	PKIKP		768.55	0.927	11.51	2.77	38.86	= PKIKP
38.86 2739.0	SKIKS		991.66	0.984	6.46	1.75	38.86	= SKIKS

38.86 2689.0	p		361.78	4.684	-82.06	14.14	38.86	= p
38.86 2689.0	PcP		370.05	4.110	60.34	12.38	38.86	= PcP
38.86 2689.0	s		663.69	8.761	-80.08	15.82	38.86	= s
38.86 2689.0	SKS		680.34	7.590	58.58	13.66	38.86	= SKS
38.86 2689.0	ScS		680.40	7.675	59.64	13.82	38.86	= ScS
38.86 2689.0	PKIKP		772.15	0.924	11.76	2.76	38.86	= PKIKP
38.86 2689.0	SKIKS		998.52	0.982	6.34	1.75	38.86	= SKIKS

38.86 2639.0	p		361.37	4.763	-81.63	14.39	38.86	= p
38.86 2639.0	PcP		371.94	4.067	57.64	12.25	38.86	= PcP
38.86 2639.0	s		662.56	8.926	-80.75	16.12	38.86	= s
38.86 2639.0	SKS		684.04	7.591	57.08	13.66	38.86	= SKS
38.86 2639.0	ScS		684.04	7.593	57.10	13.67	38.86	= ScS
38.86 2639.0	PKIKP		775.77	0.920	11.02	2.75	38.86	= PKIKP
38.86 2639.0	SKIKS		1005.41	0.980	6.22	1.75	38.86	= SKIKS

38.86 2589.0	p		360.93	4.860	-82.71	14.69	38.86	= p
38.86 2589.0	PcP		374.00	4.026	55.24	12.12	38.86	= PcP
38.86 2589.0	s		661.50	9.093	-81.49	16.44	38.86	= s
38.86 2589.0	ScS		687.93	7.515	54.82	13.52	38.86	= ScS
38.86 2589.0	PKIKP		779.41	0.917	10.79	2.74	38.86	= PKIKP
38.86 2589.0	SKIKS		1012.32	0.978	6.11	1.74	38.86	= SKIKS

38.86 2539.0	p		360.52	4.962	-84.26	15.00	38.86	= p
38.86 2539.0	PcP		376.18	3.986	53.07	12.00	38.86	= PcP
38.86 2539.0	s		660.54	9.254	-82.00	16.73	38.86	= s
38.86 2539.0	ScS		692.06	7.441	52.78	13.39	38.86	= ScS
38.86 2539.0	PKIKP		783.07	0.914	10.56	2.73	38.86	= PKIKP
38.86 2539.0	SKIKS		1019.25	0.976	6.00	1.74	38.86	= SKIKS

11.18

10.62

3.28

3.14

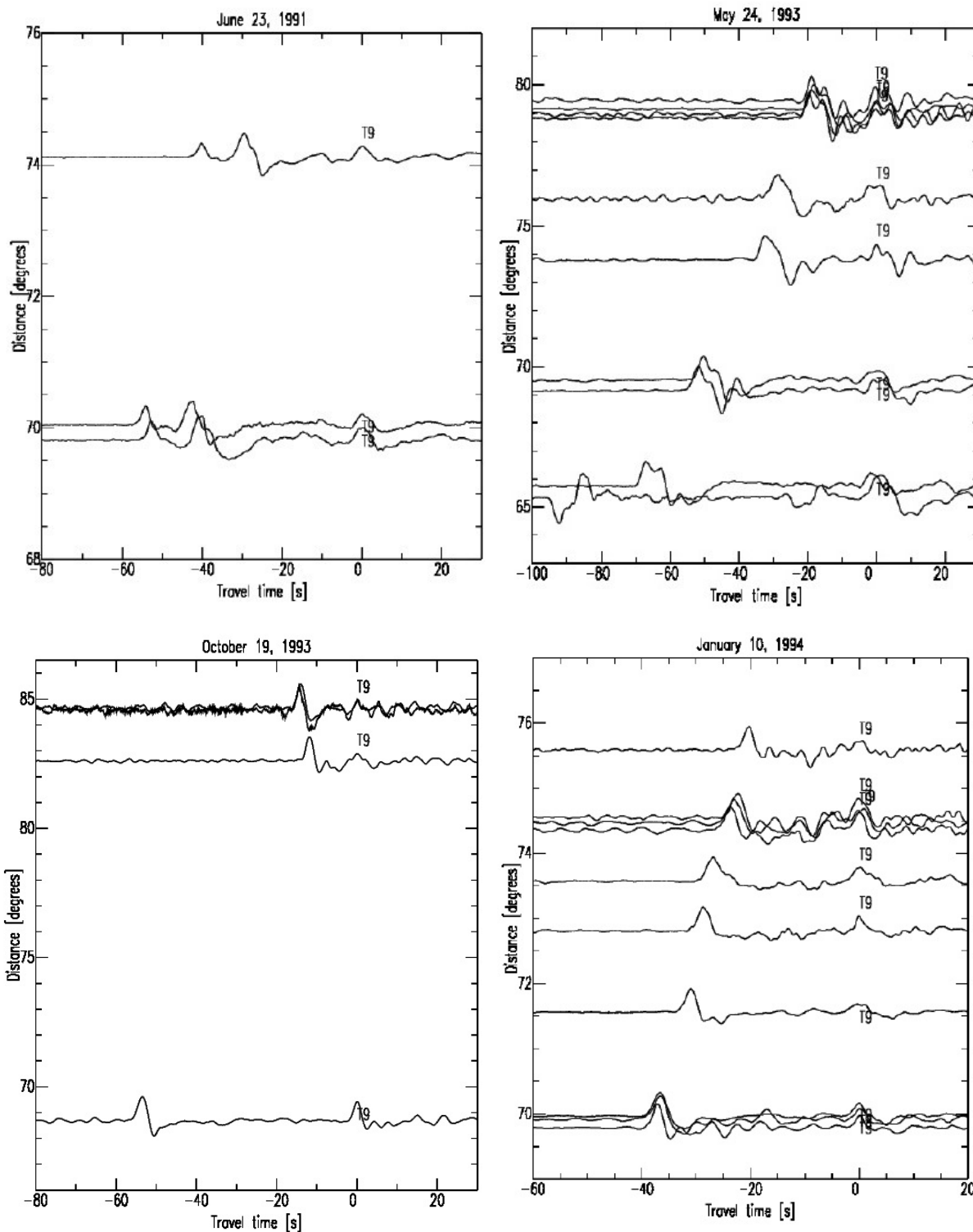
6.3

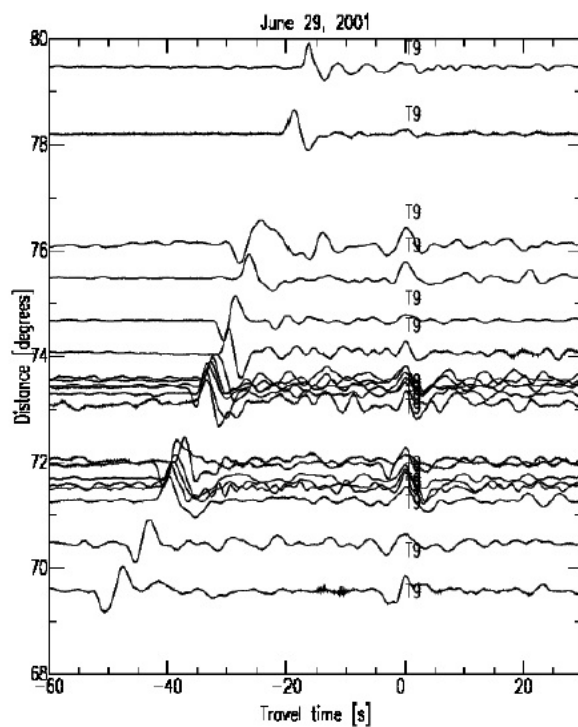
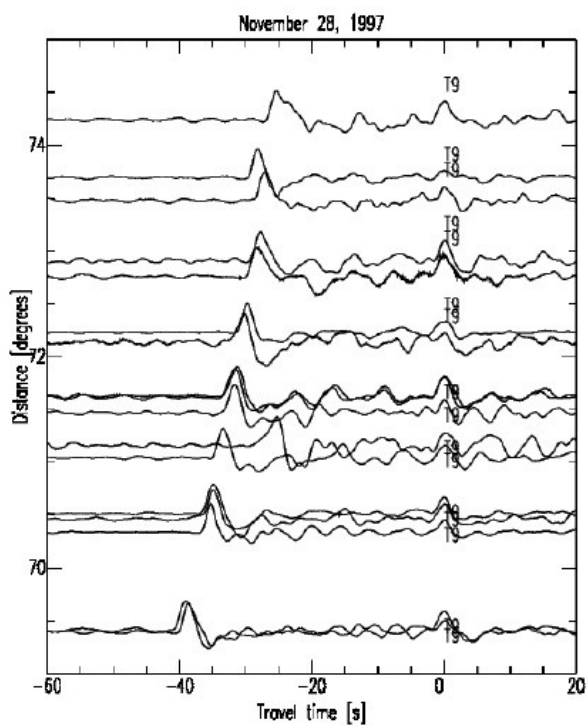
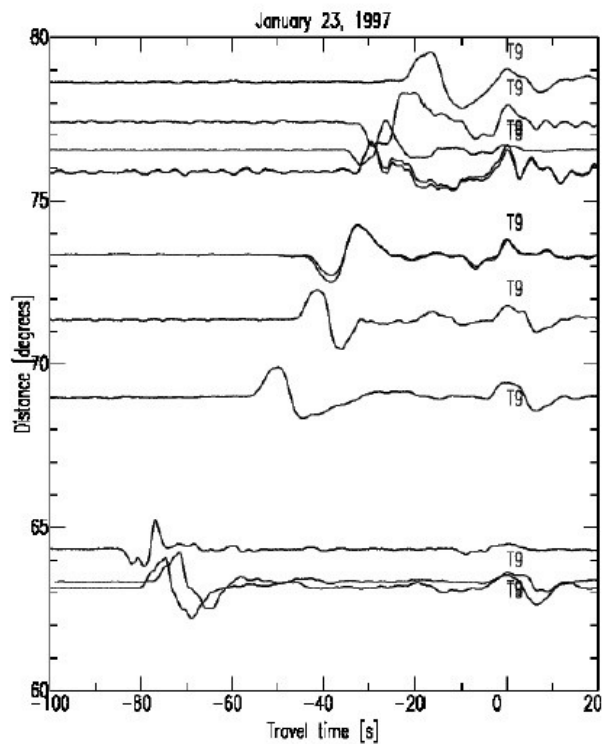
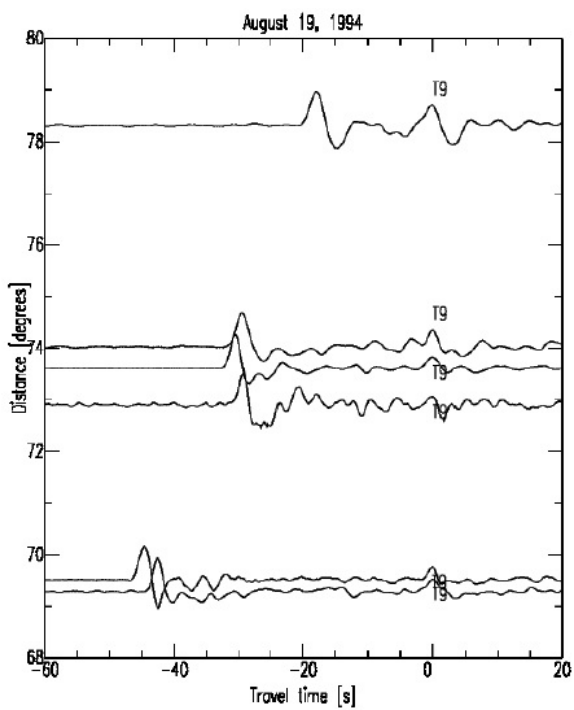
6.1

9.16



Profiles of all events 12 events in which we observed the additional SdS arrival

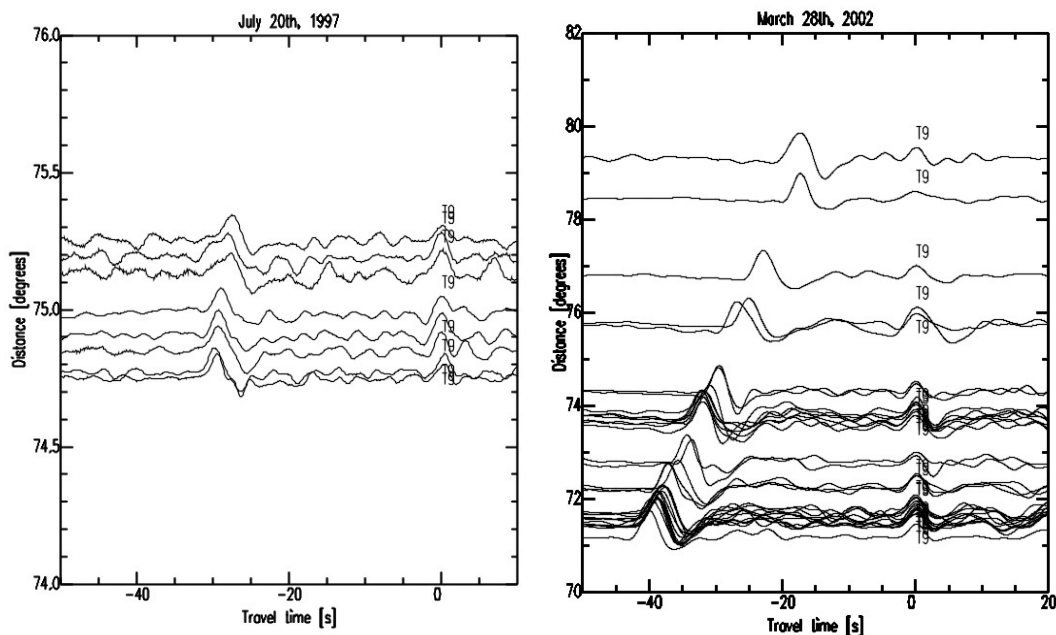




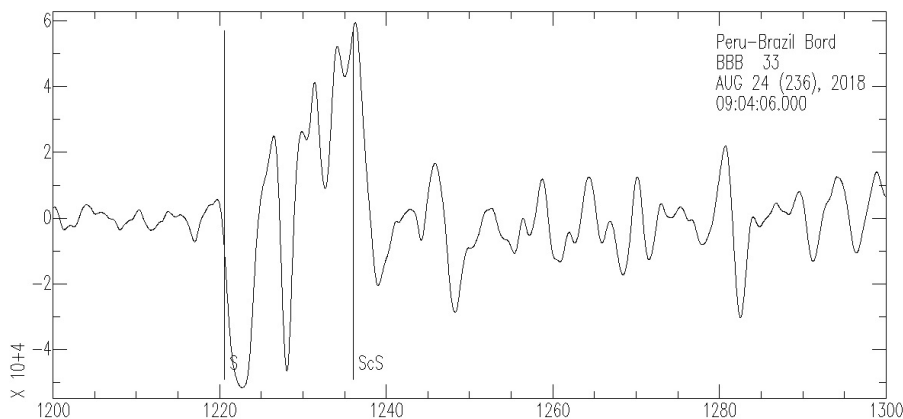


Bad data

Lastly, the profile of the events which took place in July 20th 1997 and in March 28th 2002 are also depicted below. Since the event from 1997 was a long time ago, the data is limited and there is no obvious SdS arrival present. On the other hand, the event from 2002 has more data available and there is still no SdS visible on single seismograms.



Even in the case of the events in 2007 and 2018 which are more recent and more data is available, the SdS arrival is still not visible. Some example seismograms from distances above 78 are depicted below. In the first seismogram, from the 2018 event, only the predicted S and ScS times are predicted. In this case, we can see that not even the main phases are clear, let alone the additional SdS phase. This is an example of data that is not taken into consideration for interpretation.





Below, we have plotted a seismogram from the event that took place in 2002. On the contrary to the seismogram from 2018, we can see that the main phases are really clear but there is no intermediate phase between them.

